Heat transfer through rarefied gases between coaxial cylindrical surfaces with arbitrary temperature difference

Sarantis Pantazis and Dimitris Valougeorgis[1]
Department of Mechanical Engineering
University of Thessaly, Volos 38334, Greece

Abstract

The problem of nonlinear heat transfer through a rarefied gas confined between concentric cylinders maintained at different temperatures is investigated. The formulation is based on the nonlinear Shakhov kinetic model subject to Cercignani-Lampis boundary conditions, while molecular interaction is modelled by the inverse power law. The detailed behaviour of the radial heat flow, density, temperature and pressure distributions in terms of the normalized temperature difference between the cylindrical walls, the ratio of the two cylindrical radii and the gas rarefaction is investigated and certain interesting characteristics are revealed. The study includes small, moderate and large temperature differences and various radius ratios and is extended in the whole range of the Knudsen number. It is verified that the type of molecular interaction plays an important role when the heat transfer configuration becomes strongly nonlinear, while the influence of the gas-surface scattering law has similar effects both in linear and nonlinear conditions. By comparing linear and nonlinear results corresponding to the same conditions, it is concluded that linearized analysis can capture the correct behaviour of the heat flow configuration not only for infinitesimally small but also for finite temperature differences and that its range of applicability is wider than expected.

Keywords: Knudsen number; kinetic theory; micro heat transfer; vacuum flows.

[1] Corresponding author: diva@mie.uth.gr

1. Introduction

The problem of heat transfer through rarefied gases, confined between coaxial cylindrical surfaces at different temperatures, has been theoretically investigated, based on kinetic theory, by many researchers [1-10]. However, in most cases, only small values of the normalized temperature difference are considered and linearization of the governing kinetic equations is accordingly introduced [1-5, 8, 10]. The corresponding works with a finite temperature difference are limited [6, 7, 9] and, in most cases, results are provided only within a certain range of the rarefaction, thermal and geometrical parameters involved in the problem. In addition, the influence of the implemented intermolecular potential and gas-surface interaction modelling on the macroscopic quantities are usually not considered in depth.

This simple heat transfer configuration is very common in several technological applications including the Pirani gauges [11] for monitoring pressure in vacuum technology, the multilayer insulation blankets [12] used in space vehicles and cryogenic systems and micro heat exchangers in microfluidics. Also, it has been used for a long time to determine the thermal conductivity of gases and to study temperature jump and energy accommodation at the inner cylinder.

Thus, a complete and accurate solution of the cylindrical heat transfer problem for a wide range of all involved parameters is needed. It can be obtained by solving directly a set of nonlinear kinetic equations, based on the discrete velocity (or ordinates) method, for the unknown distribution function, subject to suitable boundary conditions. Such treatment of the heat transfer problem under consideration has been successfully applied only in the case of small temperature differences based on linearized kinetic theory [10].

In the present work, the problem of heat transfer through a rarefied gas between two coaxial cylinders is solved based on the nonlinear form of the Shakhov kinetic model [13, 14], subject to Cercignani-Lampis (CL) boundary conditions [15, 16]. The Shakhov model, unlike the BGK model, provides simultaneously the correct expressions for the heat conduction and viscosity transport coefficients. Also, as it is well known, the CL scattering kernel contains two free parameters providing the possibility to distinguish between tangential momentum and normal kinetic energy accommodation. Therefore, a sufficient physical description of the gas-surface interaction is deduced. For specific values of the two parameters, the commonly used

Maxwell diffuse boundary conditions are recovered as a special case. Intermolecular interactions are simulated based on the Inverse Power Law (IPL) [17, 18]. By varying the viscosity dependence on temperature according to the IPL model, various intermolecular potentials have been considered. The two limiting cases of the IPL interaction, namely the Maxwell and the hard sphere interaction are examined in detail. The numerical solution is based on an advanced discrete velocity algorithm providing accurate results with modest computational effort. Macroscopic quantities are provided in the whole range of the Knudsen number for several values of the radius ratio and for small, moderate and large temperature differences. The influence of the gas-surface and intermolecular interaction models are investigated. The numerical results are in very good agreement with the corresponding nonlinear BGK results, provided that the collision frequency of the latter model is properly chosen to yield the correct expression for the heat conduction transport coefficient. Even more, in the case of very small temperature differences the results obtained by the nonlinear Shakhov model are in excellent agreement with previously reported results, based on the linearized Shakhov model [10]. Based on this comparison the range of validity of the linearized kinetic analysis is discussed.

2. Formulation of the problem

2.1 Cylindrical heat flow configuration and governing model equation

Consider two concentric stationary cylinders of infinite length, with radii R_A and R_B and the annular region $R_A < \hat{r} < R_B$ filled with a monatomic gas at rest and at arbitrary density level. The cylinders are maintained at different temperatures T_A and T_B, with $T_A > T_B$. Also, the cylinders are considered long and end effects in the axial direction are negligible. Due to the temperature difference $\Delta T = T_A - T_B$, which may be arbitrarily large in magnitude, there is a radial heat flow through the rarefied gas from the hot towards the cold cylinder. The problem is axially symmetric and its configuration is shown in Fig. 1, where it is seen that the letters A and B refer to the inner (hot) and outer (cold) cylinders respectively. The objective is to estimate all macroscopic distributions in terms of the three parameters governing this heat transfer

problem, namely the temperature difference between the cylindrical walls, the ratio of the two cylindrical radii and the degree of gas rarefaction.

It is convenient to introduce these three parameters in dimensionless form, taking the quantities at the outer cylinder as reference quantities. In particular

$$\beta = \frac{T_A - T_B}{T_B} \tag{1}$$

is the dimensionless temperature difference,

$$\gamma = \frac{R_A}{R_B} \tag{2}$$

is the radius ratio and

$$\delta_0 = \frac{R_B P_B}{\mu_B \upsilon_B} \sim \frac{1}{Kn_0} \tag{3}$$

is the reference rarefaction parameter. In the latter expression, P_B is the reference gas pressure, measured when the system is in equilibrium ($T_A = T_B$), μ_B is the gas viscocity at reference temperature T_B and $\upsilon_B = \sqrt{2k_B T_B / m}$, with k_B being the Boltzmann constant and m the molecular mass, is the most probable molecular velocity. The rarefaction parameter is proportional to the inverse of the Knudsen number and therefore as δ_0 is increased the atmosphere becomes more dense (or less rarefied). The cases of $\delta_0 = 0$ and $\delta_0 \to \infty$ correspond to the free molecular and hydrodynamic limits respectively.

The governing equation is the nonlinear Shakhov kinetic model, which, taking into account the symmetries of the problem under consideration, is written as [13, 14]

$$\xi_p \cos\theta \frac{\partial f}{\partial \hat{r}} - \frac{\xi_p \sin\theta}{\hat{r}} \frac{\partial f}{\partial \theta} = \frac{P}{\mu}\left(f^S - f\right), \tag{4}$$

where

$$f^S = f^M \left[1 + \frac{2m}{15n\left(k_B T\right)^2} Q \xi_p \cos\theta \left(\frac{m\xi^2}{2k_B T} - \frac{5}{2}\right)\right] \tag{5}$$

with

$$f^M = n\left(\frac{m}{2\pi k_B T}\right)^{3/2} \exp\left(-\frac{m\xi^2}{2k_B T}\right) \tag{6}$$

being the local Maxwellian. Here, $f = f\left(\hat{r}, \boldsymbol{\xi}\right)$ is the unknown distribution function, $\hat{r}$ is the radial spatial coordinate and $\boldsymbol{\xi} = \left(\xi_r, \xi_\theta, \xi_z\right) = \left(\xi_p \cos\theta, \xi_p \sin\theta, \xi_z\right)$ is the molecular velocity vector, while $\boldsymbol{\xi}_p = \left(\xi_r, \xi_\theta\right)$, shown in Fig. 1, is the planar velocity vector, with $\xi_p = \left|\boldsymbol{\xi}_p\right|$. Also, n, T and Q are the macroscopic distributions of number density, temperature and radial heat flow respectively, which may be obtained by the moments of the distribution function according to

$$n\left(\hat{r}\right) = \int\int\int f \xi_p d\xi_p d\theta d\xi_z \tag{7}$$

$$T\left(\hat{r}\right) = \frac{m}{3n\left(\hat{r}\right)k_B} \int\int\int \left(\xi_p^2 + \xi_z^2\right) f \xi_p d\xi_p d\theta d\xi_z \tag{8}$$

and

$$Q\left(\hat{r}\right) = \frac{m}{2} \int\int\int \left(\xi_p^2 + \xi_z^2\right)\left(\xi_p \cos\theta\right) f \xi_p d\xi_p d\theta d\xi_z \,, \tag{9}$$

Furthermore, μ is the viscocity of the gas at local temperature T, while P is the local pressure of the gas given by the equation of state

$$P = nk_B T \,. \tag{10}$$

It is noted that, even though the Shakhov model fulfils the collision invariants and provides correct expressions of the transport coefficients, there is no proof so far that it satisfies the H-theorem. This is a drawback for the Shakhov model. However, this unresolved issue produces no numerical problems or unphysical findings (e.g. negative distributions). Furthermore, it has been chosen between several nonlinear kinetic models, mainly due to the fact that the corresponding linearized solution for the specific heat transfer problem is available in the literature [10], allowing a direct comparison between the linear and nonlinear solutions at small temperature differences. This is important, in order to benchmark the nonlinear results in the linear limit and also to check the range of validity of the linearized theory. As mentioned before, all results are in good agreement with the corresponding nonlinear BGK results provided that in the BGK model

$$\xi_p \cos\theta \frac{\partial f}{\partial \hat{r}} - \frac{\xi_p \sin\theta}{\hat{r}} \frac{\partial f}{\partial \theta} = \nu\left(f^M - f\right) \tag{11}$$

the collision frequency is accordingly chosen as $\nu = (2P)/(3\mu)$ in order to obtain the correct heat conduction transport coefficient.

2.2 Reduced non-dimensional kinetic equations and quantities

The unknown distribution function introduced in the previous section depends on four independent variables (one in the physical space and three in the velocity space). Following a typical projection procedure, it is possible to eliminate the $z-$component of the molecular velocity vector. By reducing the number of independent variables from four to three the associated computational effort is significantly reduced. Also, for practical reasons all equations and quantities are non-dimensionalized.

The following dimensionless quantities are introduced:

$$g\left(r,\boldsymbol{c}\right)=\frac{f\upsilon_B^3}{n_B},\ r=\frac{\hat{r}}{R_B},\ \boldsymbol{c}=\frac{\boldsymbol{\xi}}{\upsilon_B},$$

$$\rho=\frac{n}{n_B},\ \tau=\frac{T}{T_B},\ q=\frac{Q}{P_B\upsilon_B},\ p=\frac{P}{P_B}. \tag{12}$$

All quantities with the subscript B are considered as reference quantities. Here, $g\left(r,\boldsymbol{c}\right)$ is a dimensionless distribution function, with $\gamma\le r\le 1$ and $\boldsymbol{c}=\left(c_r,c_\theta,c_z\right)$ denoting the independent variables ($c_r=\zeta\cos\theta$, $c_\theta=\zeta\sin\theta$), while ζ denotes the magnitude of the dimensionless molecular planar velocity vector. Furthermore, ρ, τ, q, and p are the dimensionless distributions of number density, temperature, radial heat flow and gas pressure respectively.

Then, to proceed with the mathematical manipulation, molecular interaction must be specified. The IPL interaction, where the repulsive force between two molecules is proportional to the inverse of the $n-$th power of the distance between their centers, is introduced. The IPL interaction yields a viscocity of the form [17, 18]

$$\mu=\mu_B\left(T/T_B\right)^{\omega}, \tag{13}$$

where $\omega=1/2+\left[2/\left(n-1\right)\right]$. The parameter ω takes the values of $1/2$ and 1 for the hard sphere ($n\to\infty$) and Maxwell ($n=5$) interactions respectively, which are the two limiting cases. Based on the above it is easily deduced that the local rarefaction parameter, defined as $\delta=\left(PR_B\right)/\left(\mu\upsilon\right)$, is given by

$$\delta=\delta_0\rho\tau^{1-\omega}, \tag{14}$$

where δ_0 is the reference rarefaction parameter defined in Eq. (3).

The quantities given by Eqs. (12) and (14) are introduced into Eqs. (4-6), to yield the dimensionless nonlinear Shakhov kinetic model equation

$$\zeta\cos\theta\frac{\partial g}{\partial r}-\frac{\zeta\sin\theta}{r}\frac{\partial g}{\partial\theta}=\delta_0\rho\tau^{1-\omega}\left(g^S-g\right), \tag{15}$$

where

$$g^S=g^M\left[1+\frac{4}{15}\frac{1}{\rho\tau^2}q\zeta\cos\theta\left(\frac{c^2}{\tau}-\frac{5}{2}\right)\right], \tag{16}$$

with

$$g^M=\frac{\rho}{\left(\pi\tau\right)^{3/2}}\exp\left(-c^2/\tau\right) \tag{17}$$

being the dimensionless local Maxwellian. Since the Shakhov collision model satisfies, as it should, the collisional invariants of mass, momentum and energy, the corresponding conservation equations may be obtained by operating accordingly on Eq. (15). The detailed derivation is contained in Appendix A. The mass equation implies that $u(r)=0$ is always satisfied, while the energy equation yields that the product $q(r)r$ is constant at any position $\gamma\le r\le 1$ between the cylinders. Both conditions are implemented to benchmark the accuracy of the computed distribution function. Also, from the $r-$momentum equation it is deduced that the gradient dp/dr is different than zero. Thus, there is a pressure gradient due to heat flow and not due to fluid flow. This is a non-equilibrium cross effect, which becomes stronger as the temperature difference between the cylinders and the gas rarefaction are increased, while it is completely eliminated in the hydrodynamic limit.

Next, the projection procedure is introduced by defining the reduced distribution functions

$$\phi(r,\zeta,\theta)=\int g dc_z \quad \text{and} \quad \psi(r,\zeta,\theta)=\int c_z^2 g dc_z\,. \tag{18}$$

Then, by operating successively on Eq. (15-17) with the integral operators $\int(.)dc_z$ and $\int(.)c_z^2dc_z$, the following two coupled integro-differential equations are obtained for the unknowns ϕ and ψ:

$$\zeta\cos\theta\frac{\partial\phi}{\partial r}-\frac{\zeta\sin\theta}{r}\frac{\partial\phi}{\partial\theta}=\delta_0\rho\tau^{1-\omega}\left(\phi^S-\phi\right) \tag{19}$$

$$\zeta\cos\theta\frac{\partial\psi}{\partial r}-\frac{\zeta\sin\theta}{r}\frac{\partial\psi}{\partial\theta}=\delta_0\rho\tau^{1-\omega}\left(\psi^S-\psi\right) \tag{20}$$

Here,

$$\phi^S = \phi^M \left[1 + \frac{4}{15} \frac{1}{\rho\tau^2} q\zeta \cos\theta \left(\frac{\zeta^2}{\tau} - 2 \right) \right] \tag{21}$$

and

$$\psi^S = \psi^M \left[1 + \frac{4}{15} \frac{1}{\rho\tau^2} q\zeta \cos\theta \left(\frac{\zeta^2}{\tau} - 1 \right) \right], \tag{22}$$

while

$$\phi^M = \frac{\rho}{\pi\tau} \exp\left(-\zeta^2/\tau\right) \qquad \text{and} \qquad \psi^M = \frac{\rho}{2\pi} \exp\left(-\zeta^2/\tau\right) \tag{23}$$

are the local Maxwellians. The same non-dimensionalization and projection procedures are applied to the moments (7-9), to find that the macroscopic quantities are given, in terms of ϕ and ψ, according to

$$\rho(r) = \int_0^{2\pi} \int_0^{\infty} \phi \zeta \, d\zeta \, d\theta \,, \tag{24}$$

$$\tau(r) = \frac{2}{3\rho(r)} \int_0^{2\pi} \int_0^{\infty} \left(\zeta^2 \phi + \psi \right) \zeta \, d\zeta \, d\theta \tag{25}$$

and

$$q(r) = \int_0^{2\pi} \int_0^{\infty} (\zeta \cos\theta) \left(\zeta^2 \phi + \psi \right) \zeta \, d\zeta \, d\theta \,. \tag{26}$$

Also, gas pressure is given by $p(r) = \rho(r)\tau(r)$. Equations (19-23), along with the associated moments (24-26) constitute the basic set of equations to be solved.

2.3 The Cercignani-Lampis boundary conditions

Having established the set of governing equations, we turn next to the important issue of deriving the appropriate boundary conditions for the outgoing distributions at the inner ($r = \gamma$) and outer ($r = 1$) walls. In general, the boundary conditions are imposed using the expression [14]

$$|\xi_n| \, f(\boldsymbol{\xi}) = \int_{\xi_n' < 0} |\xi_n'| R(\boldsymbol{\xi}' \to \boldsymbol{\xi}) \, f(\boldsymbol{\xi}') \, d\boldsymbol{\xi}' \,. \tag{27}$$

The prime superscript denotes particles impinging to the surface, while un-primed quantities concern the departing molecules. The n subscript refers to the direction normal to the wall surface. The symbol $R(\boldsymbol{\xi}' \to \boldsymbol{\xi})$ represents the scattering kernel,

i.e. the probability density for a molecule approaching a wall with velocity $\boldsymbol{\xi}'$ and being reflected with velocity $\boldsymbol{\xi}$.

In the present work the CL scattering kernel is implemented [15, 16, 19] and it is written as

$$R\left(\boldsymbol{\xi}' \to \boldsymbol{\xi}\right) = \frac{m^2 \xi_n}{2\pi\alpha_n\alpha_t\left(2-\alpha_t\right)\left(k_B T_w\right)^2} \exp\left\{-\frac{m\left[\xi_n^2 + \left(1-\alpha_n\right)\xi_n'^2\right]}{2k_B T_w \alpha_n}\right\} \exp\left\{-\frac{m\left[\boldsymbol{\xi}_t - \left(1-\alpha_t\right)\boldsymbol{\xi}_t'\right]^2}{2k_B T_w \alpha_t\left(2-\alpha_t\right)}\right\} I_0\left(\frac{\sqrt{1-\alpha_n}\, m\xi_n\xi_n'}{\alpha_n k_B T_w}\right) \tag{28}$$

Here, T_w is a wall temperature and $I_0(x) = \frac{1}{2\pi}\int_0^{2\pi} \exp(x\cos\varphi) d\varphi$ is the modified Bessel function of the first kind and zeroth order and the t subscript refers to the direction tangential to the wall surface. As it is seen, the CL model includes two free parameters, namely $0 < \alpha_t \le 2$ and $0 < \alpha_n \le 1$, which are the accommodation coefficients of tangential momentum and kinetic energy due to the normal molecular velocity, respectively. In the cases of $\alpha_t = \alpha_n = 1$ and $\alpha_t = \alpha_n = 0$, the CL scattering kernel is reduced to the purely diffuse and specular Maxwell scattering kernels, respectively. Even more, the so-called backscattering, which may be present on particularly rough surfaces, can be simulated with $\alpha_t \to 2$ and $\alpha_n \to 0$. For various values of α_t and α_n, the model produces lobular distributions of the re-emitted particles, which are in good agreement with molecular beam experiments [15]. Overall, it provides a reasonable physical description of the gas-surface interaction. Over the years, the CL model has been successfully applied in rarefied gas dynamics [20-25].

So far most of the work has been based on the linearized CL model. The reduced nonlinear CL boundary conditions, implemented in the present work, are formulated as follows. First, Eq. (27) and (28) are non-dimensionalized according to Eq. (12) and then the projection procedure on the resulting equations, as defined by the integral expressions (18), is introduced. After applying this mathematical manipulation the following boundary conditions for the outgoing reduced distribution functions are deduced at the inner wall ($r = \gamma$):

$$\phi(\gamma,\zeta,\theta) = -\frac{2}{\alpha_n\left(1+\beta\right)^{3/2}\sqrt{\pi\alpha_t\left(2-\alpha_t\right)}} \int_{\pi/2}^{3\pi/2}\int_0^{\infty} \left(\zeta'\cos\theta'\right)\phi\left(\gamma,\zeta',\theta'\right)$$

$$\exp\left[-\frac{(\zeta\cos\theta)^2+(1-\alpha_n)(\zeta'\cos\theta')^2}{(1+\beta)\alpha_n}\right]\exp\left[-\frac{\left[(\zeta\sin\theta)-(1-\alpha_t)(\zeta'\sin\theta')\right]^2}{(1+\beta)\alpha_t(2-\alpha_t)}\right]$$

$$I_0\left[\frac{2\sqrt{1-\alpha_n}(\zeta'\cos\theta)(\zeta'\cos\theta')}{(1+\beta)\alpha_n}\right]\zeta' d\zeta' d\theta' \qquad (29)$$

$$\psi(\gamma,\zeta,\theta)=-\frac{2}{\alpha_n(1+\beta)^{3/2}\sqrt{\pi\alpha_t(2-\alpha_t)}}\int_{\pi/2}^{3\pi/2}\int_0^{\infty}(\zeta'\cos\theta')\left[(1-\alpha_t)^2\psi(\gamma,\zeta',\theta')+\frac{1+\beta}{2}\alpha_t(2-\alpha_t)\phi(\gamma,\zeta',\theta')\right]$$

$$\exp\left[-\frac{\left((\zeta\cos\theta')\cos\theta\right)^2+(1-\alpha_n)\left((\zeta'\cos\theta')\cos\theta'\right)^2}{(1+\beta)\alpha_n}\right]\exp\left[-\frac{\left[(\zeta\sin\theta)-(1-\alpha_t)\left((\zeta'\cos\theta')\sin\theta'\right)\right]^2}{(1+\beta)\alpha_t(2-\alpha_t)}\right]$$

$$I_0\left[\frac{2\sqrt{1-\alpha_n}(\zeta\cos\theta)(\zeta'\cos\theta')}{(1+\beta)\alpha_n}\right]\zeta' d\zeta' d\theta' \qquad (30)$$

The above expressions are valid for $\theta\in[-\pi/2,\pi/2]$.

It is noted that, even though gas-surface interaction is correctly described with the CL model, the involved computational effort is significantly increased. Thus, for the present heat transfer problem, only purely diffuse boundary conditions ($\alpha_t=\alpha_n=1$) are applied on the outer wall ($r=1$). This choice is also justified by the fact that one of the main purposes of this heat transfer configuration is to provide a methodology for determining the accommodation coefficients of the filament. Thus, a technical surface with no exceptional treatment would suffice for the outer cylinder and, as a result, purely diffuse boundary conditions should be adequate. Moreover, a larger impact of the scattering kernel is expected on the inner cylinder due to temperature variation. Based on the above, the following boundary conditions are applied for the reduced distribution functions at the outer wall ($r=1$):

$$\phi(1,\zeta,\theta)=\frac{1}{\pi}\exp\left(-\zeta^2\right) \qquad (31)$$

$$\psi(1,\zeta,\theta)=\frac{1}{2\pi}\exp\left(-\zeta^2\right) \qquad (32)$$

The above expressions are valid for $\theta\in[\pi/2,3\pi/2]$.

The nonlinear set of Eqs. (19-26) along with the boundary conditions (29-32) provide a theoretically well-established kinetic formulation for the heat transfer problem under consideration.

3. Computational scheme

Both the molecular velocity space (ζ,θ), with $\zeta\in[0,\infty)$ and $\theta\in[0,2\pi]$, and the physical space $r\in[\gamma,1]$ are discretized. The continuum spectrum of magnitudes of the molecular velocity vector is replaced by a set of discrete magnitudes $\zeta_m\in[0,\zeta_{\max}]$, $m=1,2,...,M$, which are taken to be the roots of the Legendre polynomial of order M accordingly mapped from $[-1,1]$ to $[0,\zeta_{\max}]$. It is obvious that the choice of this discrete set is directly connected to the implemented numerical integration over the molecular velocity space. Although, various discrete velocity sets may be applied, it has been found that the Gauss-Legendre integration provides reliable results with less computational effort in the whole range of the Knudsen number without changing the integration rule depending upon the gas rarefaction. The numerical parameters related to the choice of the discrete velocity magnitudes used in the present work are provided in Table 1. Also, by using a uniform grid, the angular space is divided into N intervals. Each of the angular intervals is defined by its angle θ_n, $n=1,2,...,N$. Finally, the distance between the two cylinders is divided into I equal segments, defined by r_i, $i=1,2,...,I+1$.

The governing kinetic Eqs. (19) and (20) are discretized in the variable ζ and the resulting equations are integrated over each spatial and angular interval, $[r_{i-1/2},r_{i+1/2}]$ and $[\theta_{n-1/2},\theta_{n+1/2}]$. The first and the second term at the left hand side of the kinetic equations are integrated analytically in terms of r and θ respectively and then the integration in terms of the remaining variable is performed based on the trapezoidal rule. The resulting discrete equation for ϕ is

$$\phi_{m,n+\frac{1}{2},i+\frac{1}{2}}\left[\frac{\zeta_m\cos\theta_n}{2\Delta r}-\frac{\zeta_m\sin\theta_n}{2r_{i+\frac{1}{2}}\Delta\theta}+\frac{\delta_0}{4}\rho_{i+\frac{1}{2}}\tau^{1-\omega}_{i+\frac{1}{2}}\right]+\phi_{m,,n-\frac{1}{2},i+\frac{1}{2}}\left[\frac{\zeta_m\cos\theta_n}{2\Delta r}+\frac{\zeta_m\sin\theta_n}{2r_{i+\frac{1}{2}}\Delta\theta}+\frac{\delta_0}{4}\rho_{i+\frac{1}{2}}\tau^{1-\omega}_{i+\frac{1}{2}}\right]+$$

$$\phi_{m,n+\frac{1}{2},i-\frac{1}{2}}\left[-\frac{\zeta_m\cos\theta_n}{2\Delta r}-\frac{\zeta_m\sin\theta_n}{2r_{i-\frac{1}{2}}\Delta\theta}+\frac{\delta_0}{4}\rho_{i-\frac{1}{2}}\tau^{1-\omega}_{i-\frac{1}{2}}\right]+\phi_{m,n-\frac{1}{2},i-\frac{1}{2}}\left[-\frac{\zeta_m\cos\theta_n}{2\Delta r}+\frac{\zeta_m\sin\theta_n}{2r_{i-\frac{1}{2}i}\Delta\theta}+\frac{\delta_0}{4}\rho_{i-\frac{1}{2}}\tau^{1-\omega}_{i-\frac{1}{2}}\right]=$$

$$=\frac{\delta_0}{4}\left[\rho_{i+\frac{1}{2}}\tau^{1-\omega}_{i+\frac{1}{2}}\left(\phi^S_{m,n+\frac{1}{2},i+\frac{1}{2}}+\phi^S_{m,n-\frac{1}{2},i+\frac{1}{2}}\right)+\rho_{i-\frac{1}{2}}\tau^{1-\omega}_{i-\frac{1}{2}}\left(\phi^S_{m,n+\frac{1}{2},i-\frac{1}{2}}+\phi^S_{m,n-\frac{1}{2},i-\frac{1}{2}}\right)\right], \qquad (33)$$

where

$$\phi^{S}_{m,n,i}=\left[1+\frac{4}{15}\frac{1}{\rho_i\tau_i^2}q_i\zeta_m\cos\theta_n\left(\frac{\zeta_m^2}{\tau_i}-2\right)\right]\frac{\rho_i}{\pi\tau_i}\exp\left(-\zeta^2/\tau_i\right). \tag{34}$$

The corresponding equation for ψ is derived in a similar manner and is omitted here. Due to the trapezoidal integration, the error is of $O\left(\Delta r^2,\Delta\theta^2\right)$ and its form is known.

The discretized equations for $\phi_{m,,n,i}$ and $\psi_{m,,n,i}$ and the associated discretized moments (24-26) for ρ_i, τ_i and q_i are solved in an iterative manner. Based on the computed values of ρ_i, τ_i and q_i of the previous iteration (or on a reasonable initial assumption at the beginning), the kinetic equations are solved for $\phi_{m,,n,i}$ and $\psi_{m,,n,i}$. Then, updated values of ρ_i, τ_i and q_i are obtained by introducing in the moments the computed distribution functions. The new values of the bulk quantities are used to initiate the next iteration. This iteration process is terminated when some convergence criteria imposed on the macroscopic quantities is fulfilled and is named in this text the typical iteration algorithm. The flow diagram of this algorithm is shown in Fig. 2.

The typical iteration algorithm has been upgraded by implementing the Romberg integration rule and the Wynn-epsilon (We) acceleration algorithm [27, 28]. In particular, the Romberg rule provides very accurate estimates of integration in the macroscopic quantities and in the boundary conditions, even when coarse angle and spatial grids are used, while the We algorithm speeds up the slow convergence of the typical iteration scheme. Both methodologies result to a significant reduction of CPU time. The flow diagram of the upgraded algorithm is shown in Fig. 3.

The Romberg integration rule is carried out by the expression

$$T_k\left(m\right)=\frac{4^kT_{k-1}\left(2m\right)-T_{k-1}\left(m\right)}{4^k-1},\qquad k=1,2,3...\,, \tag{35}$$

where $T_k\left(m\right)$ denotes the estimation of an integral with m intervals after k integration steps, while $T_0\left(m\right)$ is the original trapezoidal rule with m intervals. This treatment can be implemented in both the spatial and angular domains and the resulting accuracy is of $O\left(\Delta r^{2k+2},\Delta\theta^{2k+2}\right)$. The Romberg rule is applied twice. First, at the Cercignani-Lampis boundary conditions (29) and (30), when integration with respect to the angle θ, is performed. The trapezoidal estimates are obtained initially on a coarse grid of n angles, which is doubled repeatedly until the total number of N angles is reached. Secondly, at the macroscopic quantities (24-26), where the

computation is performed initially on a coarse spatial and angular grid and, after convergence has been reached, it is repeated in a refined mesh, where the grid parameters have been doubled. This refinement is repeated $k-1$ times and the results are combined according to Eq. (35) at each spatial point until the final number of N angles and I space nodes is reached.

It is also noted that in each grid refinement the results of the previous grid have been used as an initial condition to speed up convergence. This procedure has lead to an accurate solution with a moderately dense grid. In particular, the initial number of angular and spatial intervals are $N=24$ and $I=51$ respectively. Then, the Romberg rule is applied four times ($k=5$) in the angular space and two times ($k=3$) in the physical space, leading to the final values of $N=192$ and $I=201$. The above parameters are used for all values of the rarefaction parameter δ_0

The We acceleration is a strongly nonlinear sequence accelerator that can exhibit spectacular acceleration for some sequences and has been described as the most elegant of all convergence acceleration methods [29]. The convergence of a series S_j, $j=1,...,J$, can be accelerated by forming a tableau whose even columns are estimations of the sequence limit

$$\varepsilon_{l+1}^{(j)} = \varepsilon_{l-1}^{(j+1)} + \left[\varepsilon_l^{(j+1)} - \varepsilon_l^{(j)} \right]^{-1}, \tag{36}$$

with $\varepsilon_{-1}^{(j)} = 0$ and $\varepsilon_0^{(j)} = S_j$. This algorithm is imposed inside the typical iteration loop to all macroscopic quantities, ρ_i, τ_i and q_i. Thus, a value of each sequence is stored in regular intervals between the iterations and a transitional stage is allowed before each application of the algorithm. It is important to numerically monitor the values of each sequence and ensure that the series is converging. Then, the We acceleration is implemented. If the series is diverging then the We acceleration is not used within this iteration loop and the last estimation obtained by the typical iterative scheme is kept. Also, in general, the upgraded iterative method with the We acceleration scheme is stable and converges in the whole range of the δ. Attention is needed in the hydrodynamic regime, where the parameters of the We scheme must be chosen after some numerical trials in order to optimize performance. In the calculations, a total of $J=51$ terms have been used for $\delta_0 \le 200$ and $J=101$ for $\delta_0 > 200$.

Comparing the computational efficiency of the typical and the upgraded algorithms it has been found that while keeping the same accuracy in the results, the CPU time of the latter one is reduced by at least one order of magnitude. Furthermore, both Romberg and We schemes are easily applied in both linearized and nonlinear kinetic problems. Finally, it is noted that for more demanding problems the upgraded algorithm can be further improved by extending and optimizing the implementation of the Romberg rule.

4. Results and discussion

Results in graphical and tabulated form are presented for the macroscopic quantities in terms of all parameters involved in the problem. In particular, in Section 4.1 the radial heat flow as well as the distributions of temperature, density and pressure are provided for various values of the normalized temperature difference β, the radius ratio γ and the reference rarefaction parameter δ_0. The influence of the type of the gas-surface interaction and the intermolecular collision models on the macroscopic quantities, are examined in Sections 4.2 and 4.3 respectively. Finally, in Section 4.4 the range of validity of the linear solution is considered by comparing the present nonlinear results with the corresponding linearized ones for various values of β.

The numerical results presented here, are based on the discretization and the numerical parameters given in Section 3. This set of parameters ensures grid independent results to all three significant figures given in the tables below. Validation of the numerical solution and benchmarking of the results has been performed in several manners. The numerical results satisfy the conservation equations obtained in Appendix A with at least 0.01% accuracy, while in the free molecular and hydrodynamic limits, they coincide with the analytical solutions presented in Appendix B. Also, for all cases examined the obtained results based on the nonlinear Shakhov model are in very good agreement with the corresponding ones obtained by the nonlinear BGK model, provided that the proper collision frequency is implemented in the BGK model. In addition, for adequately small temperature differences the nonlinear solution provides identical results to several significant figures with the corresponding linearized ones. Finally, additional benchmarking has been performed by considering the limiting case of γ being very close to one, which

corresponds to the problem of heat transfer between two parallel plates. Very good agreement has been obtained between the present results with the radius ratio $\gamma = 0.999$ and the corresponding ones for the plane heat transfer problem.

4.1 Bulk quantities for hard sphere molecules with diffuse boundary conditions

In this subsection the study is focused on the dependency of the macroscopic quantities on δ_0, γ and β. Therefore, only diffuse boundary conditions ($\alpha_t = \alpha_n = 1$) and hard sphere molecules ($\omega = 1/2$) are considered. The reference rarefaction parameter varies in the whole range of the Knudsen number ($0 \le \delta_0 \le 650$), the outer radius is 2 up to 65 times larger than the inner radius ($1/2 \le \gamma \le 1/65$), while the normalized temperature difference takes the values of $\beta = 0.1$, 1 and 10. The temperature ratio is $T_A / T_B = 1 + \beta$. It may be stated that the values of $\beta = 0.1$, 1 and 10 correspond to linear, nonlinear and strongly nonlinear heat transfer configurations respectively.

First, results for the radial heat flow, a quantity with great practical interest defined by Eq. (26), are presented. As it is noted before, if the radial heat flow is defined at some point $\gamma \le r \le 1$, then based on the energy conservation principal (the product $q(r)r$ remains constant), it may be easily calculated at any point along the radius using the relation $q(\gamma)\gamma = q(r)r = q(1)$. Therefore, most of the results and discussion are based on the estimation of $q(r)$ at $r = \gamma$.

The behaviour of the radial heat flow $q(r = \gamma)$ in terms of the reference rarefaction parameter δ_0 is shown in Fig. 4 for $\gamma = 0.1$, 0.2, 0.5 and $\beta = 0.1$, 10. It is seen that in most cases as δ_0 is increased (i.e., the gas becomes more dense) the dimensionless radial heat flow is decreased monotonically. In particular, it is decreased very slowly for $\delta_0 < 1$, while the reduction becomes much faster for $\delta_0 > 1$. However, it is seen that in the case of $\beta = 10$ and $\gamma = 0.1$, starting from $\delta_0 = 10^{-2}$ the heat flow is slightly increased, reaching a peak in the transition regime around $\delta_0 \simeq 1$, and then it is decreased as δ_0 is increased. This is a nonlinear effect appearing at large β and small γ. Overall it is obvious that the gas rarefaction strongly influences the radial heat flow for all values of β and γ.

The radius ratio effect can also be noticed in Fig. 4. It is seen that in the free molecular regime $0 \le \delta_0 \le 0.1$ the radial heat flow is independent of γ for both small and large temperature differences. Then, as δ_0 is increased the effect of γ on q becomes more evident. In particular, for $\delta_0 \ge 0.1$, q is decreased as γ is increased (i.e. as the annular region is decreased).

The behaviour of the radial heat flow $q(r=\gamma)$ in terms of β is shown in Table 2, covering a wide range of all three parameters determining the heat transfer problem. For small values of β the radial heat flow is increased proportionally to β. However, as β is increased and in particular for $\beta \ge 1$ the dependency is not linear any more and q is increased faster, following a power law of β. It is also seen that this nonlinear behaviour becomes stronger as the rarefied gas becomes denser, i.e. as δ_0 is increased. It may be useful to note that tabulated results are important in this type of research work since they can be easily accessed in the future for comparison purposes with experiments or as benchmarks for computations. In this framework, the results of Table 2 will be used in the next subsections in order to study the influence of the intermolecular interaction law and the type of gas-surface interaction on the heat transfer characteristics. In addition, they will also be used to study the range of validity of the linear approximation by comparing with corresponding linear results previously reported in the literature. In order to provide this comparison in a direct manner, we have chosen to provide the heat flow results in Table 2 in terms of β, γ and the product $\delta_0\gamma$. It is readily seen that the values of the rarefaction parameter in Table 2 vary in $0 \le \delta_0 \le 650$.

Next, the macroscopic quantities of number density and temperature, defined by Eqs. (24) and (25) respectively, are considered. In Fig. 5, the temperature distributions $\tau(r)$ of the gas are presented along the radius $\gamma \le r \le 1$ for $\beta = 0.1$, 1, 10, $\gamma = 0.1$, 0.5 and various values of δ_0. It is noted that the dimensionless temperature of the inner ($r=\gamma$) and outer ($r=1$) cylindrical wall is $\tau_A = 1+\beta$ and $\tau_B = 1$ respectively. It is clearly seen that the temperature jump at the walls is increased as δ_0 is decreased. It is also observed that the temperature jump at the inner wall is significantly larger than the corresponding jump at the outer wall. Even more, as β is increased the temperature jumps at both walls are increased. However, it is evident from the plotted

results that the increase of β has a much stronger effect on the jump at the inner compared to that of the outer wall. To illustrate this significant impact of β on $\tau(\gamma)$ it is stated that in the free molecular limit ($\delta_0 = 0$) for $\beta = 1$ the temperature of the wall is $\tau_A = 2$ and the temperature of the gas at the wall is $\tau(\gamma) = 1.4$. The corresponding values for $\beta = 10$ are $\tau_A = 11$ and $\tau(\gamma) = 3.3$. This behaviour may be explained by the fact that the gas becomes more rarefied as its temperature is increased. Beyond the quantitative differences, the qualitative behaviour of the temperature profiles with regard to β is similar. Comparing the temperature profiles for $\gamma = 0.5$ and 0.1 it is seen that the temperature is decreased more rapidly in the latter case.

The dimensionless number density distributions $\rho(r)$ are shown in Fig. 6 for $\beta = 0.1$, 1, 10, $\delta_0 = 0$, 2, 20 and $\gamma = 0.5$. As expected, the values of the number density are low at the hot wall and high at the cold wall, while they are monotonically increased between the two walls. This is in agreement with the related characteristics of the temperature distributions discussed above. Also, in all cases the density distributions have the common S-shaped profile, except in the case of $\beta = 10$ and $\delta_0 = 20$. The latter behaviour is a nonlinear effect and it is present at large β and δ_0. Since, according to Eq. (14) in the cases of hard sphere and Maxwell molecules, $\delta = \delta_0 \rho \sqrt{\tau}$ and $\delta = \delta_0 \rho$ respectively, the variation of the local rarefaction parameter between the cylinders is qualitatively similar to that of the density profiles in Fig. 6. Thus, moving from the hot towards the cold wall the rarefaction parameter is monotonically increased, i.e. the atmosphere becomes less rarefied.

The dimensionless pressure profile is also plotted in Fig. 7 for $\beta = 0.1$, 1, 10, $\gamma = 0.1$, 0.5 and various values of δ_0. Although the pressure distribution may be directly obtained by the density and temperature distributions, $p = \rho\tau$, it is plotted for completeness and clarity purposes. It is seen that, in all cases, there is a pressure variation along the radius of the annulus, which is increased as δ_0 is decreased and β is increased. This observation has been theoretically proven in Appendix A and it has been also observed by other researchers [4, 8]. The pressure variation is quite small for $\beta = 0.1$ and this is the reason that it has not been reported before in all related

papers based on linear analysis. Of course for $\beta=1$ and 10 the pressure variation is significant and there is no way to be due to numerical error. The build-up of a pressure gradient due to an imposed heat flow is sparkled by non-equilibrium conditions and becomes more profound at large temperature differences and highly rarefied atmospheres.

4.2 Influence of intermolecular interaction law

The influence of the intermolecular interaction on the heat transfer characteristics is studied through the variation of the IPL coefficient. The radial heat flow and temperature distributions are plotted in Fig. 8 for hard spheres ("HS") and Maxwell molecules ("MM") characterized by $\omega=0.5$ and $\omega=1$ respectively. Results are provided for $\gamma=0.5$, $\beta=0.1$, 10 and $\delta_0=0$, 2, 20. As expected, the corresponding results are identical in the free molecular limit ($\delta_0=0$). For $\delta_0>0$ it is deduced that the variation between the "HS" and "MM" results is negligibly small at $\beta=0.1$ even for large values of δ_0. However, the discrepancies are significant at $\beta=10$, particularly for $\delta_0=20$. Observing the heat flow distributions it is seen that the heat flow results of the "MM" are always higher than the corresponding ones for the "HS". Comparing the temperature distributions of the two types of molecules it is deduced that at both walls the temperature jumps of the "MM" are always larger than the ones of the "HS". Therefore, the corresponding distributions are crossing each other somewhere along the annular radius closer to the cold wall.

In addition, tabulated results of the radial heat flow $q(r=\gamma)$ for Maxwell molecules are given in Table 3 for a wide range of the involved parameters. The results of Table 3 can be compared directly with the ones in Table 2 for hard spheres. This comparison confirms that the deviation between corresponding "HS" and "MM" results is enlarged as β and δ_0 are increased and that it is also increased as γ is decreased (i.e. the annular region becomes larger). Indicatively, it is reported that for $\gamma=0.1$ and $\delta_0=10$ ($\delta_0\gamma=1$) the relative error is 4% at $\beta=1$ and 14% at $\beta=10$, while the maximum deviation between the reported results in Tables 2 and 3, which is 58%, occurs at $\beta=10$, $\gamma=1/65$ and $\delta_0=650$.

To extend this analysis beyond the limiting "HS" and "MM" molecules, in Fig. 9, some dimensional radial heat flow results (W/m^2) in terms of the reference pressure

P_B (Pa) are given for three different monoatomic gases, namely helium, argon and xenon having under standard conditions $\omega = 0.66$, 0.81 and 0.85. These results are provided in dimensional form in order to facilitate comparisons with experiments in the short future. The inner and outer diameters are $R_A = 1cm$ and $R_B = 10cm$, while the reference temperature is $T_B = 293K$. The reference pressure and the type of the gas are easily related to the reference rarefaction parameter δ_0, while in order to keep these results as general as possible, the other two parameters β and γ are kept in dimensionless form. As expected, at highly rarefied atmospheres the heat flow is proportional to the gas pressure, while at dense atmospheres the heat flow becomes independent of the gas pressure. When the gas pressure is in the transition regime the relation is complex.

4.3 Influence of gas-surface interaction

The influence of the gas-surface interaction law on the radial heat flow is studied by providing numerical results for $q(r=\gamma)$ in terms of the parameters $0<\alpha_t \le 2$ and $0<\alpha_n \le 1$ of the Cercignani-Lampis boundary conditions, which are applied at the inner wall and Maxwell diffuse boundary conditions ($\alpha_t = 1, \alpha_n = 1$) at the outer wall. The results are for the hard sphere model and for various values of β, γ and δ_0.

In Fig. 10, the radial heat flow $q(r=\gamma)$ is plotted for $\beta = 1$ and $\gamma = 0.5$ in terms of each accommodation coefficient while keeping each time the other one constant and equal to unity. It is clearly observed that the dependency of q on α_t is weak, while, on the contrary, its dependency on α_n is significant. Even more, as expected in both cases, as δ_0 is decreased the effect of the accommodation coefficients becomes stronger. It is also noted that the radial heat flow in terms of α_t is symmetric around $\alpha_t = 1$. This property is inherent in the form of the boundary conditions (29) and (30). Values of $\alpha_t > 1$ correspond to large number of bouncing-back molecules, which happens at rough surfaces. In terms of α_n, q is monotonically increased. It is obvious, that α_n is more important than α_t in pure heat transfer problems. The same features are observed for other values of β. Furthermore, the behavior of the

macroscopic quantities in terms of the two accommodation coefficients is qualitatively similar in linear and nonlinear configurations.

Since the implementation of the CL boundary conditions is demanding in terms of formulation and numerical implementation and in order to increase our confidence on the accuracy of the present numerical solution based on the nonlinear Shakhov model, the results reported here are compared with previously reported results for the same heat transfer configuration based on the linearized Shakhov model [10]. The values of the heat flow provided in Table 4 for $\beta = 0.1$ and $\gamma = 1/65$ and for a wide range of α_t and α_n may be directly compared with the corresponding results of Table IV in Ref. [10]. The values of $\delta_0 \gamma$ and δ in the first columns of Table 4 and Table IV respectively are equivalent. Since the normalized temperature difference is small ($\beta = 0.1$), it is expected to have good agreement between the present nonlinear results and the corresponding linearized ones. In fact, for $\delta_0 \gamma = 0.1$ there is agreement to all three significant figures, shown in Table 4. For $\delta_0 \gamma = 1$ the agreement is still very good since 2-3 significant figures are the same. Finally, for $\delta_0 \gamma = 10$ the agreement is reduced to 1-2 significant figures. This is reasonable since, even though $\beta = 0.1$ is a small normalized temperature difference, it is not small enough to have very accurate linearized results at large δ_0. As it is pointed out in Section 4.1 (see Table 2 and related discussion), nonlinear effects become important in dense atmospheres, even for small temperature differences.

For completeness purposes corresponding results are provided by imposing the well known Maxwell diffuse-specular scattering law at the inner wall. In Fig. 11, the radial heat flow $q(r = \gamma)$ is plotted for $\beta = 1$ and $\gamma = 0.5$ in terms of the accommodation coefficient $0 < \alpha_M \leq 1$. As expected the corresponding results in Figs. 10 and 11 for the specific values of $\alpha_n = \alpha_n = 1$ and $\alpha_M = 1$ respectively are identical. Furthermore, a qualitative remark on the comparison between Figs. 10 and 11 may be made. It is seen that the heat flows of Fig. 11 for $\delta_0 = 0$ and $\delta_0 = 20$ are similar to the corresponding ones in Fig. 10 for $\alpha_t = 1,\ 0 < \alpha_n \leq 1$ and $0 < \alpha_t \leq 1,\ \alpha_n = 1$ respectively, while for the intermediate values of $\delta_0 = 2$ and $\delta_0 = 10$ the heat flows in Fig. 11 are similar to the resulting ones obtained by a combination of the corresponding heat flows presented in Fig. 10.

4.4 Range of validity of linear analysis

The numerical treatment of linear integro-differential equations compared to the nonlinear ones is much more tractable since it is based on a well established theoretical basis. Therefore, it may be interesting to check the range of validity of the linear solution by comparing the corresponding linear and nonlinear results for various values of the normalized temperature difference parameter. According to theory, the linearization of this heat transfer problem is allowed provided that $\beta << 1$.

Results for the radial heat flow, denoted as q_L, based on the linearized Shakhov model and diffuse boundary conditions are provided for various values of δ_0 and γ in Table II of Ref. [10]. A comparison can be made with the corresponding nonlinear "HS" results, presented here in Table 2, after multiplying the linear heat flows in Table II with the appropriate value of β. As β is increased significant deviations are observed. The maximum difference for $\beta = 1$ is about 16% and for $\beta = 10$ about 64%.

The percentage error between the nonlinear and linear heat flows, defined as $\varepsilon = \left| (q - q_L)/q \right| \times 100\%$, is presented in Fig. 12 for several values of δ_0 and $\gamma = 0.1$, 0.5. In highly and moderate rarefied atmospheres ($\delta_0 = 0.2$, 2) the introduced error for all $\beta = 0.1$, 1, 10 is less than 2%. In less rarefied atmospheres ($\delta_0 = 10$, 20) the error is increased. For example for $\beta = 10$ and $\delta_0 = 20$ the error is about 15%. However, it is seen that even for large temperature differences the discrepancies remain within reasonable margins. It may be argued that the range of applicability of the linear analysis is wider than expected and this might be quite useful in practical applications.

Furthermore, the nonlinear and linear profiles of the radial heat flux and temperature are plotted in Fig. 13, for $\gamma = 0.5$, $\beta = 0.1$, 1, 10 and $\delta_0 = 0$, 2, 20. As expected, the discrepancies are very small for both quantities when $\beta = 0.1$ and then they gradually increase as β is increased. However, it is interesting to note that the discrepancies between the temperature distributions are significantly larger compared to the discrepancies of the heat flow distributions for the same set of parameters. For example, in the case of $\beta = 10$ and $\delta_0 = 20$ the deviation in the heat flow is about 15% and more or less remains constant along the radius, while the corresponding error for the temperature profiles varies along the radius and takes a maximum value of about

35% at $r = \gamma$. This is an unexpected observation, which may be important when linearized theory is applied to finite temperature differences.

5. Concluding Remarks

The problem of nonlinear heat transfer through a rarefied gas confined between two coaxial cylinders is solved based on the nonlinear form of the Shakhov kinetic model, subject to Cercignani-Lampis boundary conditions, while intermolecular interactions are simulated based on the Inverse Power Law. The governing equations are discretized based on the discrete velocity method and a typical second order finite difference scheme. The numerical algorithm becomes computationally efficient by applying the Romberg integration rule and the Wynn-epsilon (We) acceleration algorithm.

The quantitative behaviour of all macroscopic quantities (radial heat flow, density, temperature and pressure) in terms of the rarefaction parameter, the radius ratio and the temperature difference is examined in detail. A pressure variation in the radial direction is detected and confirmed. Departure of the corresponding linear results has been observed as the temperature difference between the cylinders is increased and as the gas atmosphere becomes less rarefied. This deviation becomes significant at large temperature differences and small Knudsen numbers. However, it is concluded that linear analysis can capture the correct behaviour of the heat flow configuration even for moderate temperature differences and it is argued that the range of applicability of the linear analysis is wider than expected. By studying the cases of hard sphere and Maxwell particles it is verified that the type of molecular interaction plays an important role when the heat transfer configuration becomes strongly nonlinear, while the influence of the gas-surface scattering law has similar effects both in linear and nonlinear conditions. Even more, although the formulation and most of the results are in dimensionless form, some dimensional results are also provided for specific gases in order to demonstrate in a more comprehensive manner the effect of the problem parameters on the radial heat flow.

It is hoped that the present work may be useful in engineering applications as well as in comparisons with experimental results which, as far as the authors are aware of, are not available for the case of large temperature differences at this stage.

Acknowledgments

The authors take this opportunity to thank Prof. Barry Ganapol for helpful discussions and providing some supportive material regarding the implementation of the acceleration schemes. Also, the authors gratefully acknowledge support by the Association Euratom - Hellenic Republic. The views and opinions expressed herein do not necessarily reflect those of the European Commission.

References

[1] L. Lees and C. Y. Liu, Kinetic-theory description of conductive heat transfer from a fine wire, Phys. Fluids, 5 (10), 1137-1148 (1962).

[2] C. Y. Liu, Part II: Kinetic Theory description of conductive heat transfer from a fine wire (http://etd.caltech.edu/etd/available/etd-12092005-133941/, Ph.D. thesis, California Institute of Technology, 1962).

[3] C. L. Su, Variational principals for the heat flux in a rarefied gas between concentric cylinders, Phys. Fluids, 11 (10), 2144-2147 (1968).

[4] P. Bassanini, C. Cercignani and C. D. Pagani, Influence of the accommodation coefficient on the heat transfer in a rarefied gas, Int. J. Heat Mass Transfer, 11, 1359-1369 (1968).

[5] C. L. Su and D. R. Willis, Heat conduction in a rarefied gas between concentric cylinders, Phys. Fluids, 11 (10), 2131-2143 (1968).

[6] C. L. Su and R. W. Springer, A modified discrete ordinate approach to nonlinear cylindrical heat transfer, Int. J. Heat Mass Transfer, 13, 1611-1621 (1970).

[7] Y. S. Lou and T. K. Shih, Nonlinear heat conduction in rarefied gases confined between concentric cylinders and spheres, Phys. Fluids 15 (5), 785-788 (1972).

[8] B. T. Yeh and A. Frohm, Heat conduction in binary gas mixtures between cylinders, Phys. Fluids, 16 (6), 801-805 (1973).

[9] F. Sharipov and G. M. Kremer, On the frame dependence of constitutive equations. I. Heat transfer through a rarefied gas between two rotating cylinders, Continuum Mechanics and Thermodynamics, 7, 57-71 (1995).

[10] F. Sharipov and G. Bertoldo, Heat transfer through a rarefied gas confined between two coaxial cylinders with high radius ratio, J. Vac. Sci. Technol. A, 24 (6), 2087-2093 (2006).

[11] W. Jitschin and S. Ludwig, Dynamical behavior of the Pirani sensor, Vacuum, 75, 169-176 (2004).

[12] P.J. Sun, J.Y. Wu, P. Zhang, L. Xu, M.L. Jiang, Experimental study of the influences of degraded vacuum on multilayer insulation blankets, Cryogenics, 49, 719–726 (2009).

[13] E. M. Shakhov, Generalization of the Krook kinetic relaxation equation, Fluid Dynamics, 3(5), 142-145 (1968).

[14] F. Sharipov and V. Seleznev, Data on internal rarefied gas flows, J. Phys. Chem. Ref. Data, 27(3), 657-706 (1998).

[15] C. Cercignani and M. Lampis, Kinetic models for gas-surface interactions, Transport Theory and Statistical Physics, 1(2), pp. 101-114 (1971).

[16] R. G. Lord, Some extensions to the Cercignani-Lampis gas-surface scattering kernel, Phys. Fluids A, 3 (4), 706-710 (1991).

[17] G. A. Bird, Molecular Gas Dynamics and the Direct Simulation of Gas Flows (Oxford University Press, Oxford, 1994).

[18] C. Shen, Rarefied Gas Dynamics: Fundamentals, Simulations and Micro Flows (Springer, 2005).

[19] R. G. Lord, Some further extensions to the Cercignani-Lampis gas-surface scattering kernel, Phys. Fluids, 7 (5), 1159-1161 (1995).

[20] A. Frezzotti, Numerical simulation of supersonic rarefied gas flow past a flat plate: effects of the Gas-Surface interaction model on the flow field, in Rarefied Gas Dynamics, edited by E.P.Muntz, D.P. Weaver and D.H. Campbell, (Volume 118 of Progress in Astronautics and Aeronautics, AIAA, Washington DC, 1989).

[21] F. Sharipov, Application of the Cercignani–Lampis scattering kernel to calculations of rarefied gas flows. III. Poiseuille flow and thermal creep through a long tube, Eur. J. Mech. B/Fluids, 22, 145-154 (2003).

[22] C. Cercignani, M. Lampis and S. Lorenzani, Plane Poiseuille Flow with Symmetric and Nonsymmetric Gas-Wall Interactions, Transport Theory and Statistical Physics, 33, 545-561 (2004).

[23] R. F. Knackfuss and L. B. Barichello, Surface effects in rarefied gas dynamics: an analysis based on the Cercignani–Lampis boundary condition, Eur. J. Mech. B/Fluids, 25, 113-129 (2006).

[24] W. F. N. Santos, Gas-Surface Interaction Effect on Round Leading Edge Aerothermodynamics, Brazilian Journal of Physics, 37, 337-348 (2007).

[25] R. D. M. Garcia and C. E. Siewert, The linearized Boltzmann equation with Cercignani-Lampis boundary conditions: Basic flow problems in a plane channel, Eur. J. Mech. B/Fluids, 28, 387-396 (2009).
[26] Handbook of Vacuum Technology (Chapter 5), edited by K. Jousten (Wiley-VCH Verlag, Weinheim, 2008)
[27] E. Süli and D. F. Mayers, An Introduction to Numerical Analysis (Cambridge University Press, 2003).
[28] B. D. Ganapol, Analytical Benchmarks for Nuclear Engineering Applications - Case Studies in Neutron Transport Theory (OECD, NEA No. 6292, Nuclear Energy Agency Organization for Economic Co-operation and Development, ISBN 978-92-64-99056-2, 2008).
[29] F. Borneman, A. Laurie and J. Wagen, The SIAM 100-digit Challenge (SIAM, Philadelphia, USA, 2004).
[30] C. L. Pekeris and Z. Alterman, Solution of the Boltzmann-Hilbert integral equation. II. The coefficients of viscocity and heat conduction, 43, 998-1007 (1957).

Appendix A: Conservation equations

Equation (15) is multiplied successively by 1, $\zeta\cos\theta$ and ζ^2 and the resulting equations are integrated over the molecular velocity space to yield, after some routine manipulation, the following conservation equations:

continuity $$\frac{\partial u}{\partial r}+\frac{1}{r}u_r=0 \qquad \text{(A.1)}$$

r - momentum $$\frac{\partial p_{rr}}{\partial r}+\frac{p_{rr}-p_{\theta\theta}}{r}=0 \qquad \text{(A.2)}$$

energy $$\frac{\partial}{\partial r}[qr]=0 \qquad \text{(A.3)}$$

The continuity equation, associated with the no penetration condition at the cylindrical walls, yields $u(r)=0$, while the energy equation results to $q(r)r=$ constant. Finally, since $p_{rr}\neq p_{\theta\theta}$, the r - momentum equation implies that $\partial p_{rr}/\partial r\neq 0$.

Appendix B: Solutions at the free molecular and hydrodynamic limits

In the free molecular limit ($\delta_0=0$) the right hand side of Eqs. (19) and (20) becomes zero and in the case of Maxwell diffuse boundary conditions ($\alpha_t=\alpha_n=1$) the reduced distribution functions are given for $\theta\in[-\pi/2,\pi/2]$ by

$$\phi(r,\zeta,\theta)=\frac{\rho_W}{\pi(1+\beta)}\exp\left(-\frac{\zeta^2}{1+\beta}\right),\qquad \psi(r,\zeta,\theta)=\frac{\rho_W}{2\pi}\exp\left(-\frac{\zeta^2}{1+\beta}\right) \qquad \text{(B.1)}$$

and for $\theta\in[\pi/2,3\pi/2]$ by

$$\phi(r,\zeta,\theta)=\frac{1}{\pi}\exp\left(-\zeta^2\right),\qquad \psi(r,\zeta,\theta)=\frac{1}{2\pi}\exp\left(-\zeta^2\right). \qquad \text{(B.2)}$$

where the impermeability parameter ρ_W is obtained by the no penetration condition according to

$$\rho_w=-\frac{2\sqrt{\pi}}{\sqrt{1+\beta}}\int_{\pi/2}^{3\pi/2}\int_0^\infty(\zeta\cos\theta)\phi\zeta\,d\zeta\,d\theta. \qquad \text{(B.3)}$$

Finally, by substituting these expressions into Eqs. (B.3) and (24-26) it is found that

$$\rho_w=\frac{1}{\sqrt{1+\beta}}, \qquad \text{(B.4)}$$

$$\rho(r)=\frac{1}{\pi}\left(\theta_1\frac{1}{\sqrt{1+\beta}}+\pi-\theta_1\right), \tag{B.5}$$

$$\tau(r)=\frac{1}{\rho(r)}\frac{1}{\pi}\left[\theta_1\sqrt{1+\beta}+(\pi-\theta_1)\right] \tag{B.6}$$

and

$$q(r)=\frac{\beta\gamma}{r\sqrt{\pi}}. \tag{B.7}$$

The discontinuity angle $\theta_1=\sin^{-1}(\gamma/r)$ is displayed in Fig. 1. This problem can also be solved when the Cercignani-Lampis boundary conditions are imposed on the inner cylinder. It is found that in this case the heat flux is given by

$$q(r)=\frac{\beta\gamma\left(\alpha_n+2\alpha_t-\alpha_t^2\right)}{2r\sqrt{\pi}}. \tag{B.8}$$

which is similar to the linearized case appearing in [10]. It is seen that, although the distribution function is independent of r in the free molecular limit, the macroscopic quantities still depend on the space variable. The numerical solution for $\delta_0=0$ is in excellent agreement with the analytical results of Eqs. (B.5-B.8).

In the hydrodynamic limit ($\delta_0\to\infty$) the Fourier law is introduced into the energy equation to give

$$\frac{\partial}{\partial\hat{r}}\left[k(T)\frac{\partial T}{\partial\hat{r}}\hat{r}\right]=0, \tag{B.9}$$

where, based on the IPL interaction, we have

$$k(T)=k(T_B)(T/T_B)^{\omega}. \tag{B.10}$$

Substituting Eq. (B.10) into (B.9) and nondimensionalizing the resulting equation according to Eq. (12) , leads to the temperature distribution

$$\tau(r)=\left\{\left[(1+\beta)^{\omega+1}-1\right]\frac{\ln r}{\ln\gamma}+1\right\}^{1/(\omega+1)}. \tag{B.11}$$

For hard sphere molecules, following the calculations carried out in [26, 30] it is deduced that

$$q(r)=-\frac{5}{4r}\frac{\left[(1+\beta)^{3/2}-1\right]}{\delta_0\ln\gamma}. \tag{B.12}$$

Expressions (B.11) and (B.12) are in very good agreement with numerical results for large values of δ_0 but only in cases with small temperature difference. For large β the temperature gradient at the wall becomes important and temperature jump boundary conditions must be introduced. However, the jump solution is not provided here, since the mathematical derivation becomes complex when $k = k(T)$ and ω is involved, and more important does not really support further benchmarking of the present work. In the linear case, the solution is much simpler and is given in [26].

Table 1: Number and range of discrete velocity magnitudes

β	M	$\zeta_{\max}$
0.1	20	5
1	20	6
10	24	14

Table 2: Radial heat flow $q(r=\gamma)$ for hard sphere molecules with diffuse boundary conditions

	$\delta_0\gamma$	$\gamma = 1/2$	1/5	1/10	1/20	1/65
$\beta = 0.1$	0	$5.64\ 10^{-2}$	$5.64\ 10^{-2}$	$5.64\ 10^{-2}$	$5.64\ 10^{-2}$	$5.64\ 10^{-2}$
	0.1	$5.54\ 10^{-2}$	$5.45\ 10^{-2}$	$5.38\ 10^{-2}$	$5.31\ 10^{-2}$	$5.18\ 10^{-2}$
	1	$4.73\ 10^{-2}$	$4.05\ 10^{-2}$	$3.62\ 10^{-2}$	$3.24\ 10^{-2}$	$2.72\ 10^{-2}$
	5	$2.86\ 10^{-2}$	$1.78\ 10^{-2}$	$1.36\ 10^{-2}$	$1.10\ 10^{-2}$	$8.24\ 10^{-3}$
	10	$1.90\ 10^{-2}$	$1.02\ 10^{-2}$	$7.53\ 10^{-3}$	$5.94\ 10^{-3}$	$4.40\ 10^{-3}$
$\beta = 1$	0	$5.64\ 10^{-1}$	$5.64\ 10^{-1}$	$5.64\ 10^{-1}$	$5.64\ 10^{-1}$	$5.64\ 10^{-1}$
	0.1	$5.54\ 10^{-1}$	$5.46\ 10^{-1}$	$5.39\ 10^{-1}$	$5.31\ 10^{-1}$	$5.14\ 10^{-1}$
	1	$4.73\ 10^{-1}$	$4.02\ 10^{-1}$	$3.57\ 10^{-1}$	$3.18\ 10^{-1}$	$2.68\ 10^{-1}$
	5	$2.91\ 10^{-1}$	$1.86\ 10^{-1}$	$1.45\ 10^{-1}$	$1.19\ 10^{-1}$	$9.06\ 10^{-2}$
	10	$2.00\ 10^{-1}$	$1.12\ 10^{-1}$	$8.39\ 10^{-2}$	$6.69\ 10^{-2}$	$4.97\ 10^{-2}$
$\beta = 10$	0	5.64	5.64	5.64	5.64	5.64
	0.1	5.58	5.61	5.61	5.53	5.18
	1	4.78	4.06	3.50	3.03	2.48
	5	3.04	2.04	1.63	1.37	1.10
	10	2.24	1.38	1.08	$8.95\ 10^{-1}$	$7.02\ 10^{-1}$

Table 3: Radial heat flow $q(r=\gamma)$ for Maxwell molecules with diffuse boundary conditions

	$\delta_0\gamma$	$\gamma = 1/2$	1/5	1/10	1/20	1/65
$\beta = 0.1$	0	$5.64\ 10^{-2}$	$5.64\ 10^{-2}$	$5.64\ 10^{-2}$	$5.64\ 10^{-2}$	$5.64\ 10^{-2}$
	0.1	$5.54\ 10^{-2}$	$5.45\ 10^{-2}$	$5.38\ 10^{-2}$	$5.31\ 10^{-2}$	$5.18\ 10^{-2}$
	1	$4.78\ 10^{-2}$	$4.07\ 10^{-2}$	$3.64\ 10^{-2}$	$3.26\ 10^{-2}$	$2.74\ 10^{-2}$
	5	$2.89\ 10^{-2}$	$1.80\ 10^{-2}$	$1.38\ 10^{-2}$	$1.12\ 10^{-2}$	$8.40\ 10^{-3}$
	10	$1.93\ 10^{-2}$	$1.04\ 10^{-2}$	$7.69\ 10^{-3}$	$6.07\ 10^{-3}$	$4.49\ 10^{-3}$
$\beta = 1$	0	$5.64\ 10^{-1}$	$5.64\ 10^{-1}$	$5.64\ 10^{-1}$	$5.64\ 10^{-1}$	$5.64\ 10^{-1}$
	0.1	$5.55\ 10^{-1}$	$5.47\ 10^{-1}$	$5.41\ 10^{-1}$	$5.33\ 10^{-1}$	$5.16\ 10^{-1}$
	1	$4.82\ 10^{-1}$	$4.15\ 10^{-1}$	$3.71\ 10^{-1}$	$3.33\ 10^{-1}$	$2.83\ 10^{-1}$
	5	$3.12\ 10^{-1}$	$2.06\ 10^{-1}$	$1.63\ 10^{-1}$	$1.35\ 10^{-1}$	$1.04\ 10^{-1}$
	10	$2.21\ 10^{-1}$	$1.29\ 10^{-1}$	$9.75\ 10^{-2}$	$7.85\ 10^{-2}$	$5.89\ 10^{-2}$
$\beta = 10$	0	5.64	5.64	5.64	5.64	5.64
	0.1	5.61	5.64	5.65	5.60	5.27
	1	5.09	4.52	3.99	3.50	2.91
	5	3.70	2.67	2.19	1.88	1.55
	10	2.94	1.98	1.60	1.36	1.11

Table 4: Radial heat flow $q(r=\gamma)$ with CL boundary conditions for $\beta = 0.1$ and $\gamma = 1/65$

	α_t	$\alpha_n = 0.25$	0.50	0.75	1.00
$\delta_0\gamma = 0.1$	0.50	$2.69\ 10^{-2}$	$3.33\ 10^{-2}$	$3.96\ 10^{-2}$	$4.58\ 10^{-2}$
	0.75	$3.17\ 10^{-2}$	$3.80\ 10^{-2}$	$4.42\ 10^{-2}$	$5.03\ 10^{-2}$
	0.90	$3.30\ 10^{-2}$	$3.93\ 10^{-2}$	$4.55\ 10^{-2}$	$5.16\ 10^{-2}$
	1.00	$3.32\ 10^{-2}$	$3.95\ 10^{-2}$	$4.57\ 10^{-2}$	$5.18\ 10^{-2}$
$\delta_0\gamma = 1$	0.50	$1.80\ 10^{-2}$	$2.09\ 10^{-2}$	$2.33\ 10^{-2}$	$2.55\ 10^{-2}$
	0.75	$2.01\ 10^{-2}$	$2.26\ 10^{-2}$	$2.48\ 10^{-2}$	$2.68\ 10^{-2}$
	0.90	$2.06\ 10^{-2}$	$2.31\ 10^{-2}$	$2.52\ 10^{-2}$	$2.71\ 10^{-2}$
	1.00	$2.07\ 10^{-2}$	$2.32\ 10^{-2}$	$2.53\ 10^{-2}$	$2.72\ 10^{-2}$
$\delta_0\gamma = 10$	0.50	$4.02\ 10^{-3}$	$4.16\ 10^{-3}$	$4.26\ 10^{-3}$	$4.34\ 10^{-3}$
	0.75	$4.11\ 10^{-3}$	$4.22\ 10^{-3}$	$4.31\ 10^{-3}$	$4.37\ 10^{-3}$
	0.90	$4.13\ 10^{-3}$	$4.24\ 10^{-3}$	$4.32\ 10^{-3}$	$4.38\ 10^{-3}$
	1.00	$4.14\ 10^{-3}$	$4.24\ 10^{-3}$	$4.32\ 10^{-3}$	$4.40\ 10^{-3}$

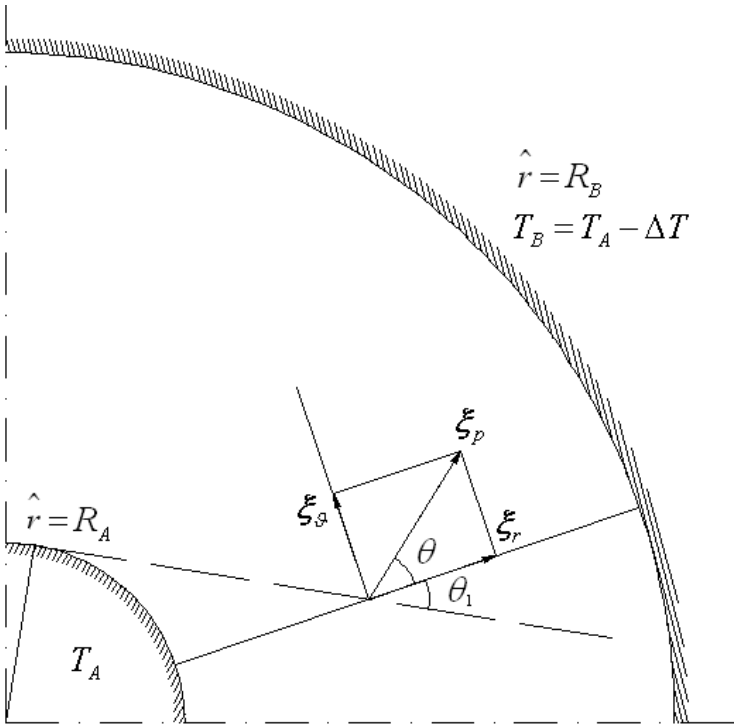

Figure 1: Heat flow configuration

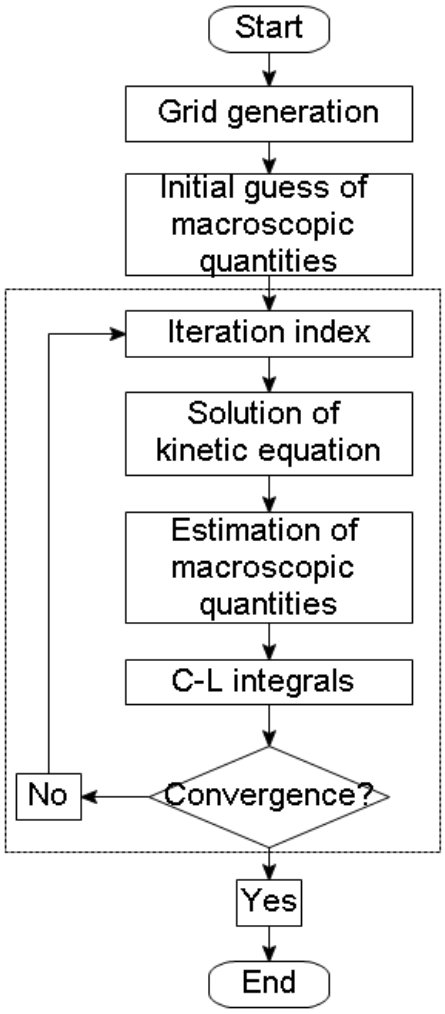

Figure 2: Flow diagram of the typical iteration algorithm

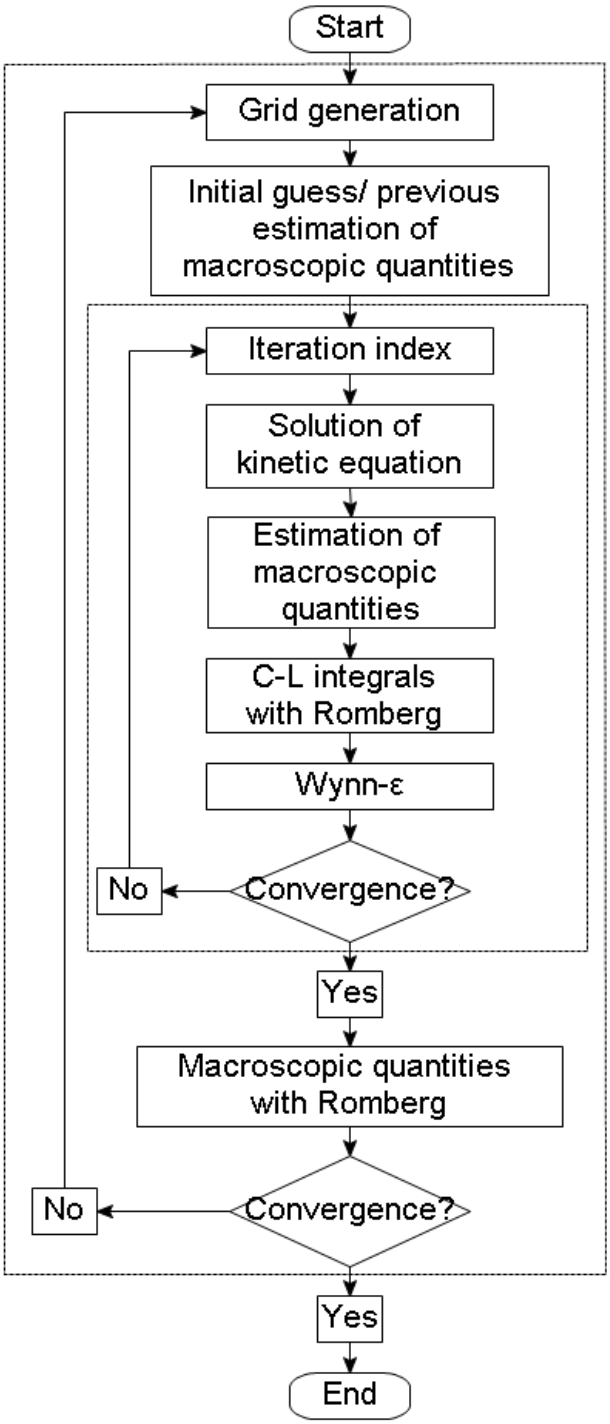

Figure 3: Flow diagram of the upgraded iteration algorithm

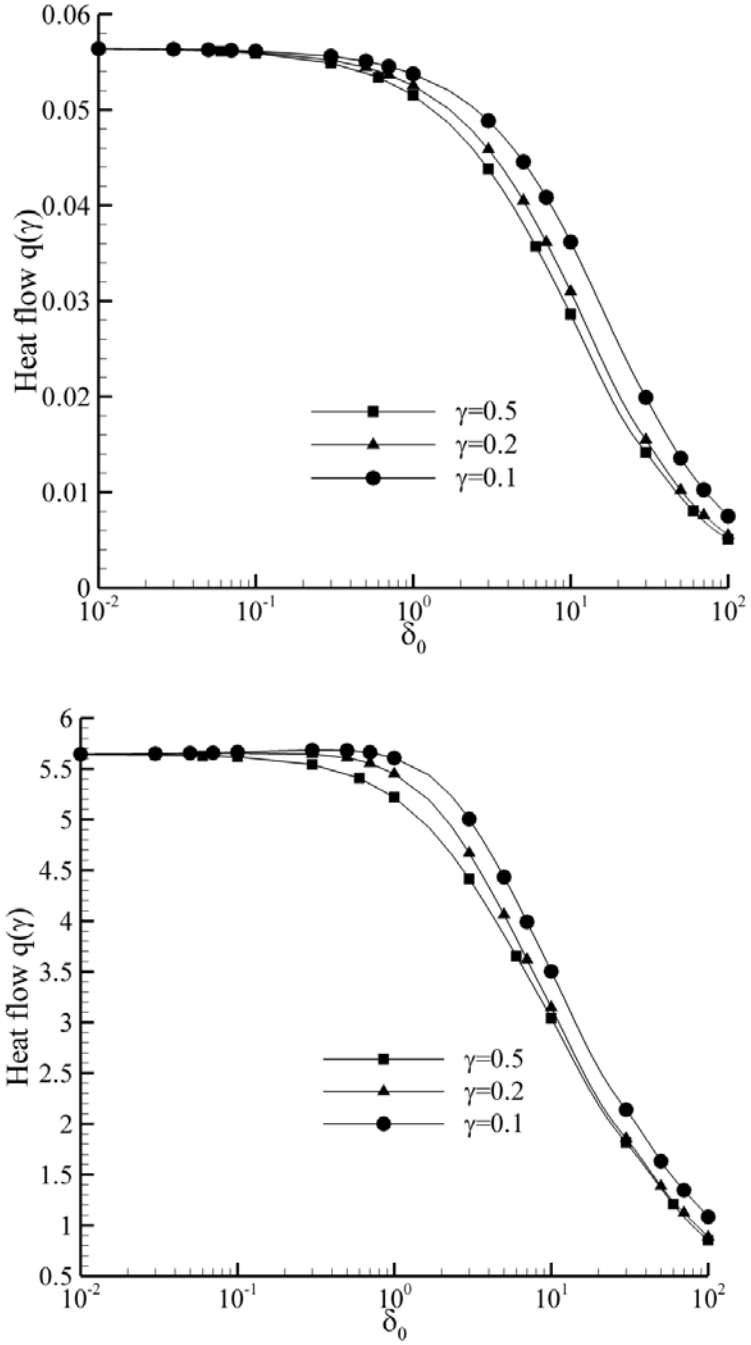

Figure 4: Dimensionless radial heat flow q at $r=\gamma$ in terms of δ_0 for various γ, with $\beta=0.1$ (up) and $\beta=10$ (down).

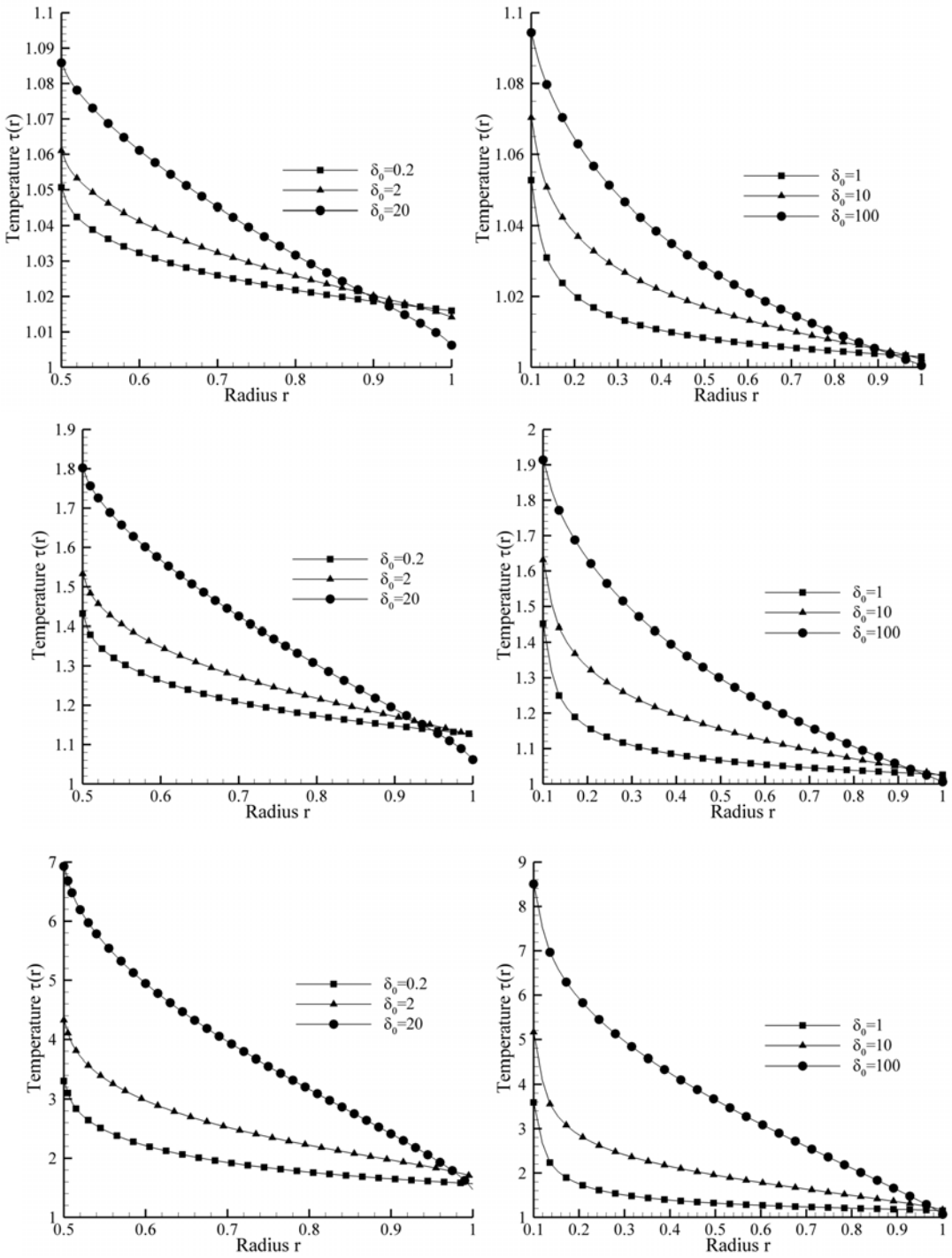

Figure 5: Dimensionless temperature profiles $\tau(r)$ for $\beta=0.1$ (up), $\beta=1$ (middle) and $\beta=10$ (down), with $\gamma=0.5$ (left) and $\gamma=0.1$ (right).

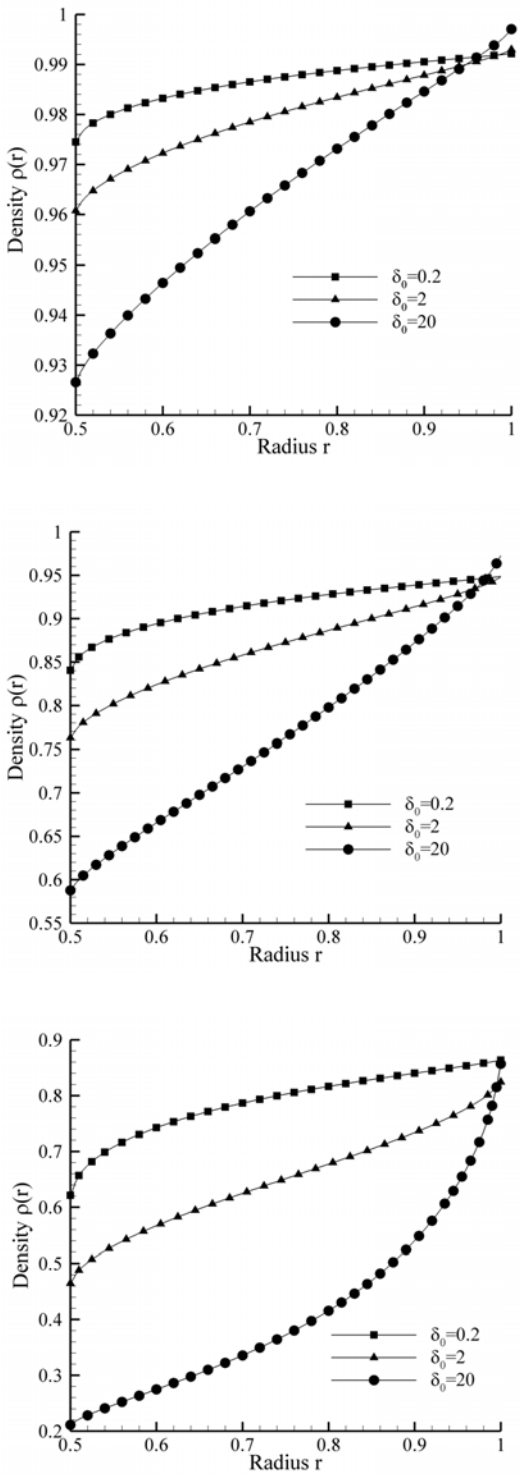

Figure 6: Dimensionless density profiles $\rho(r)$ for $\beta=0.1$ (up), $\beta=1$ (middle) and $\beta=10$ (down), with $\gamma=0.5$.

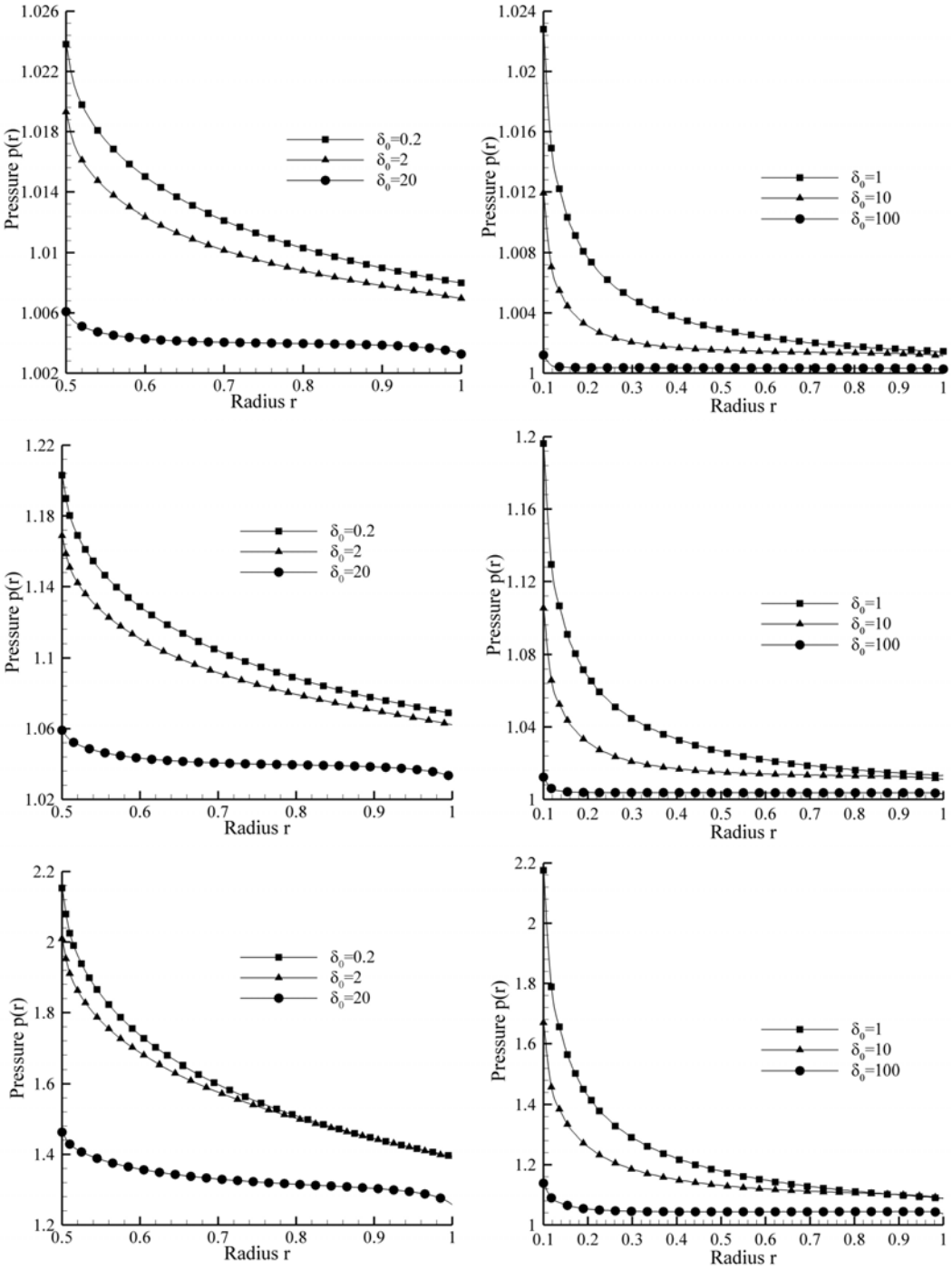

Figure 7: Dimensionless pressure profiles $p(r)$ for $\beta=0.1$ (up), $\beta=1$ (middle) and $\beta=10$ (down), with $\gamma=0.5$ (left) and $\gamma=0.1$ (right).

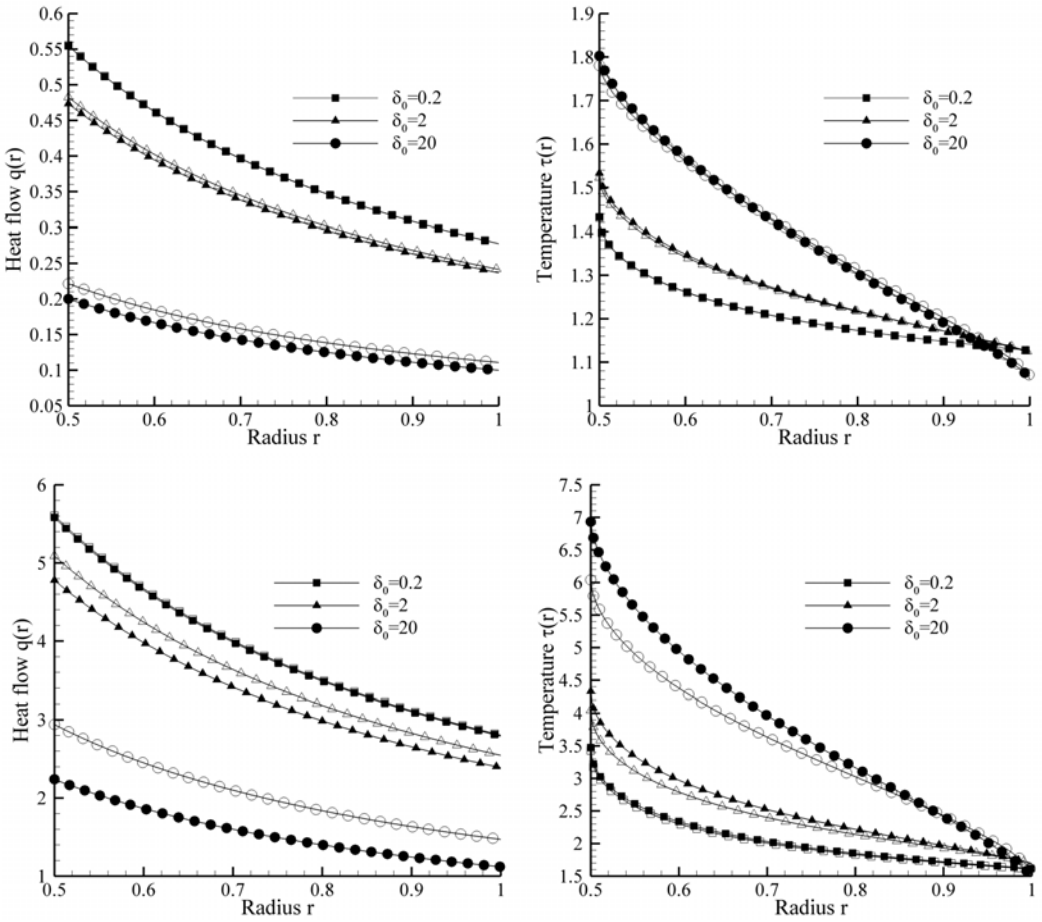

Figure 8: Dependence of the dimensionless radial heat flow and temperature distributions on the IPL coefficient ω for $\beta=1$ (up) and $\beta=10$ (down). Hard spheres $(\omega=0.5)$ are denoted with filled symbols and Maxwell molecules $(\omega=1)$ with empty symbols.

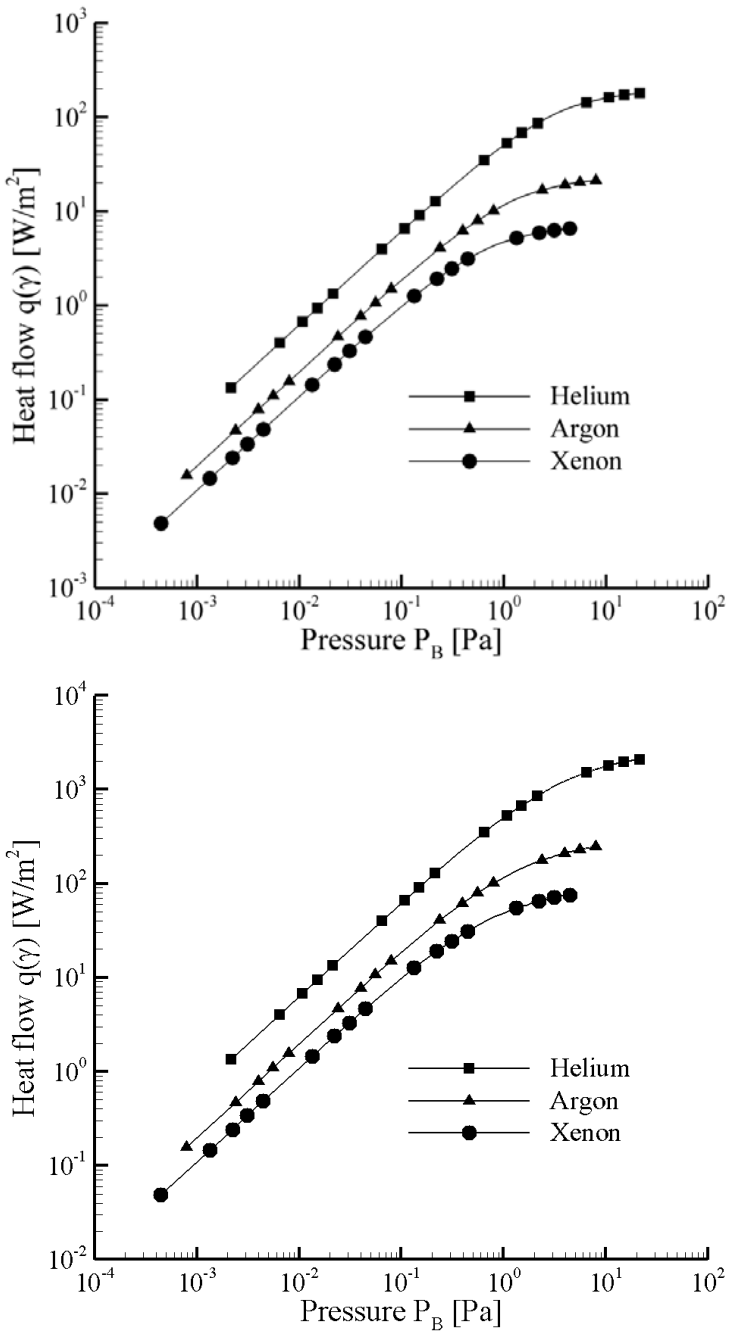

Figure 9: Dimensional radial heat flow through various gases in terms of the reference pressure P_B for $\gamma = 0.1$, with $\beta = 0.1$ (up) and $\beta = 1$ (down).

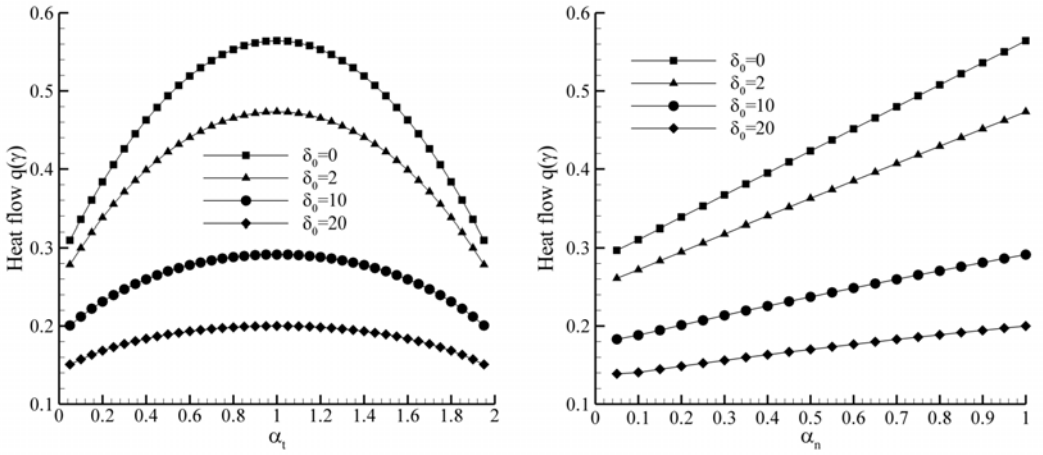

Figure 10: Dependence of the dimensionless radial heat flow on the accommodation coefficients α_t (left) and α_n (right) keeping each time the other one constant and equal to unity for $\gamma = 0.5$ with $\beta = 1$.

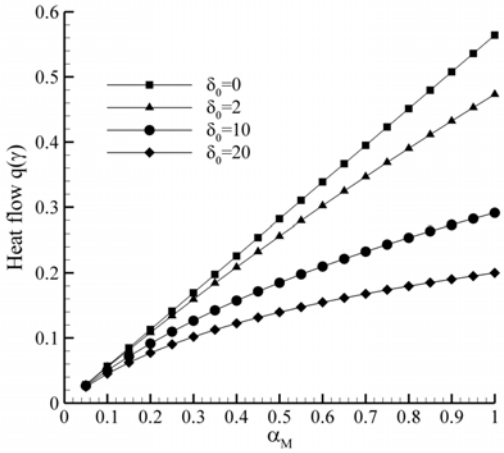

Figure 11: Dependence of the dimensionless radial heat flow on the Maxwell accommodation coefficient α_M for $\gamma = 0.5$ and $\beta = 1$.

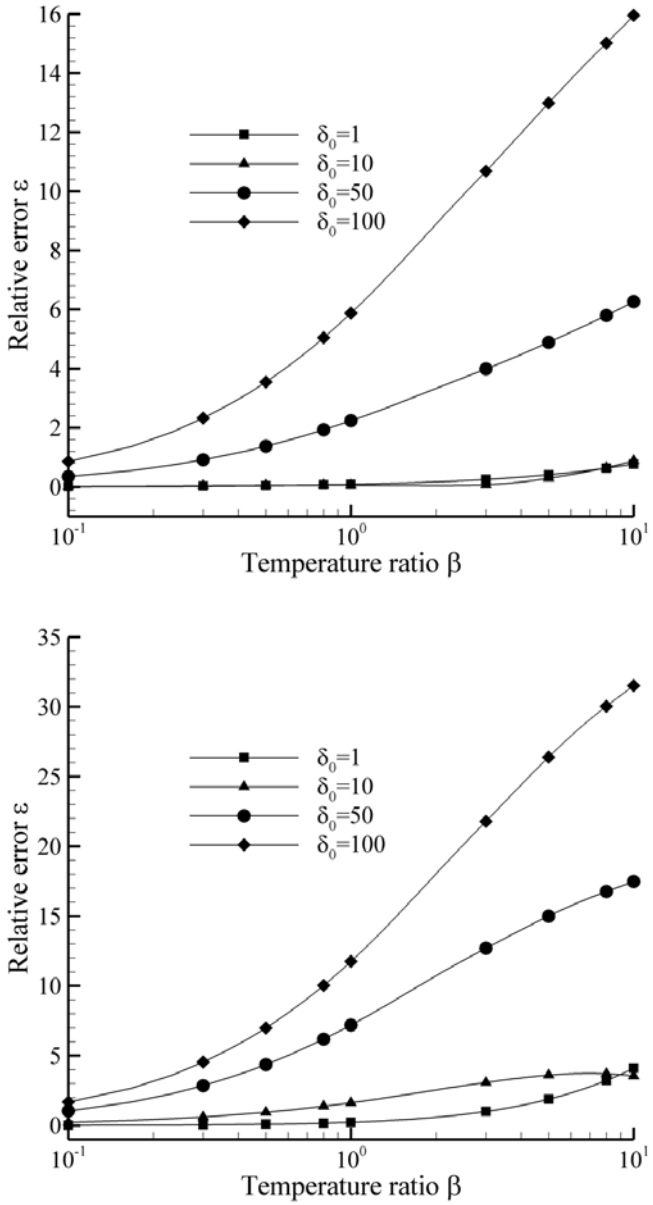

Figure 12: Relative error between nonlinear and linearized radial heat flow in terms of β for various δ_0, with $\gamma = 0.5$ (up) and $\gamma = 0.1$ (down).

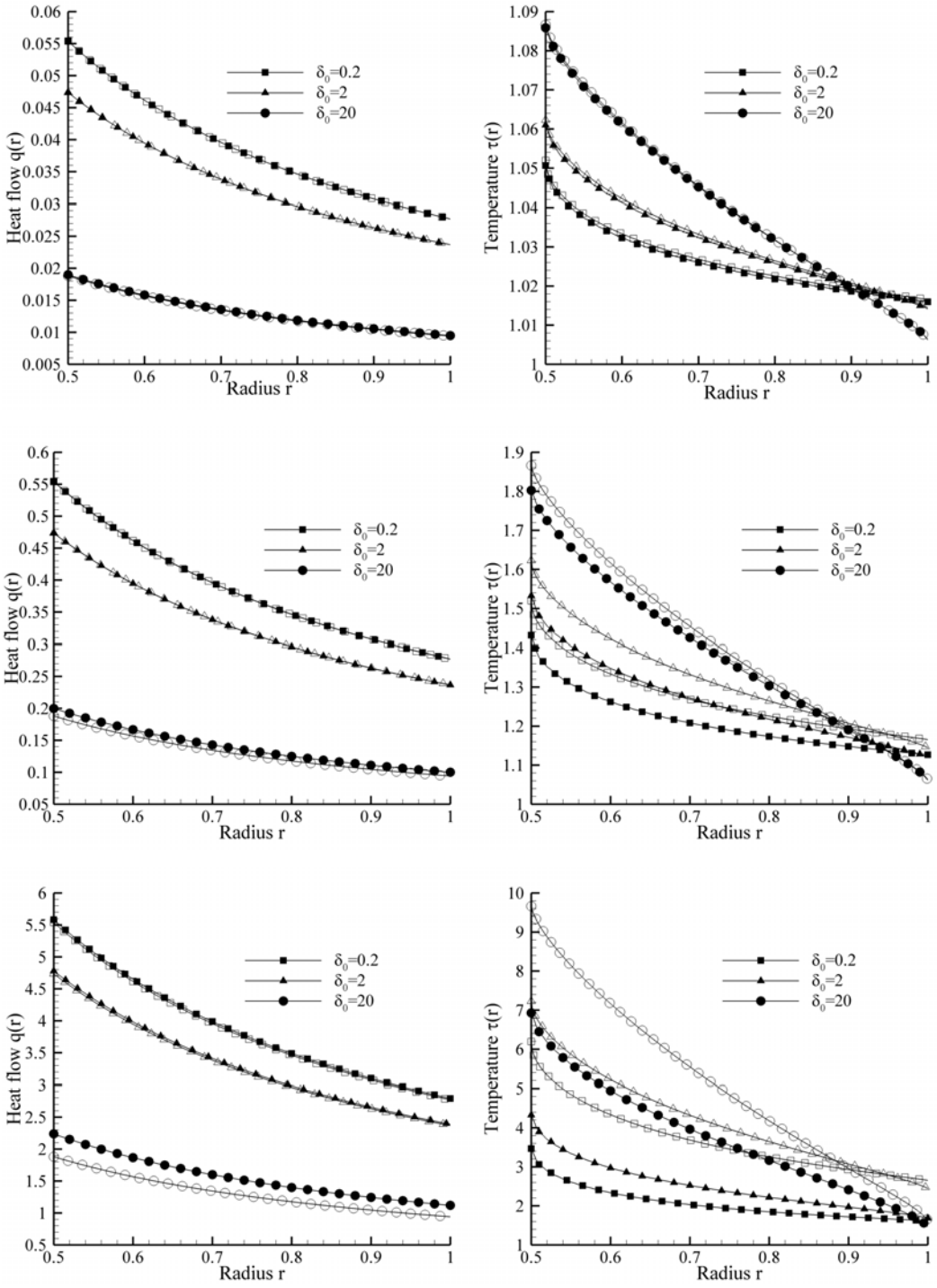

Figure 13: Dimensionless radial heat flow and temperature profiles using linearized (empty symbols) and nonlinear (filled symbols) analysis for $\beta = 0.1$ (up), $\beta = 1$ (middle) and $\beta = 10$ (down).

LIST OF FIGURES

Figure 1: Heat flow configuration.

Figure 2: Flow diagram of the typical iteration algorithm.

Figure 3: Flow diagram of the upgraded iteration algorithm.

Figure 4: Dimensionless radial heat flow q at $r=\gamma$ in terms of δ_0 for various γ, with $\beta=0.1$ (up) and $\beta=10$ (down).

Figure 5: Dimensionless temperature profiles $\tau(r)$ for $\beta=0.1$ (up), $\beta=1$ (middle) and $\beta=10$ (down), with $\gamma=0.5$ (left) and $\gamma=0.1$ (right).

Figure 6: Dimensionless density profiles $\rho(r)$ for $\beta=0.1$ (up), $\beta=1$ (middle) and $\beta=10$ (down), with $\gamma=0.5$.

Figure 7: Dimensionless pressure profiles $p(r)$ for $\beta=0.1$ (up), $\beta=1$ (middle) and $\beta=10$ (down), with $\gamma=0.5$ (left) and $\gamma=0.1$ (right).

Figure 8: Dependence of the dimensionless radial heat flow and temperature distributions on the IPL coefficient ω for $\beta=1$ (up) and $\beta=10$ (down). Hard spheres $(\omega=0.5)$ are denoted with filled symbols and Maxwell molecules $(\omega=1)$ with empty symbols.

Figure 9: Dimensional radial heat flow through various gases in terms of the reference pressure P_B for $\gamma=0.1$, with $\beta=0.1$ (up) and $\beta=1$ (down).

Figure 10: Dependence of the dimensionless radial heat flow on the accommodation coefficients α_t (left) and α_n (right) keeping each time the other one constant and equal to unity for $\gamma=0.5$, with $\beta=1$.

Figure 11: Dependence of the dimensionless radial heat flow on the Maxwell accommodation coefficient α_M for $\gamma=0.5$ and $\beta=1$.

Figure 12: Relative error between nonlinear and linearized radial heat flow in terms of β for various δ_0, with $\gamma=0.5$ (up) and $\gamma=0.1$ (down).

Figure 13: Dimensionless radial heat flow and temperature profiles using linearized (empty symbols) and nonlinear (filled symbols) analysis for $\beta=0.1$ (up), $\beta=1$ (middle) and $\beta=10$ (down).